Dissolution of (U,Th)O_2 heterogeneous mixed oxides

C. Hours, L. Claparede, N. Reynier-Tronche, I. Viallard, Renaud Podor, N. Dacheux

Dissolution of $(U,Th)O_2$ heterogeneous mixed oxides

C. Hours[1,2], L. Claparede[1], N. Reynier-Tronche[2], I. Viallard[3], R. Podor[1], N. Dacheux[1]

1 ICSM, Univ Montpellier, CNRS, CEA, ENSCM, Site de Marcoule, Bagnols sur Cèze, France.

2 CEA, DES, ISEC, DMRC, Univ Montpellier, Marcoule, France.

3 CEA, DES, IRESNE, DEC, Cadarache, France.

Corresponding author:

Laurent Claparede

ICSM, Univ Montpellier, CNRS, CEA, ENSCM

Site de Marcoule, Bat 426

30207 Bagnols sur Cèze, France

laurent.claparede@umontpellier.fr

Abstract:

Heterogeneous $U_{1-x}Th_xO_2$ polished pellets were prepared through sintering of oxides obtained from hydroxide precursors. Mixing several homogeneous $U_{1-x}Th_xO_2$ powders with various stoichiometries allowed the preparation of a panel of heterogeneous sintered pellets with a matrix-inclusions type microstructure. The characterization of the polished pellets was performed by X-EDS. From image analysis of large cartographies of the pellets, the distribution and amount of each type of heterogeneity was evaluated. To follow the chemical durability of the prepared materials, the pellets were submitted to dissolution tests in 2 and 4 $mol.L^{-1}$ HNO_3 at 60 and 90 °C. The obtained dissolution rates of the materials highlighted the need to access a more detailed microscopic study due to the presence of enriched dissolution residues at the end of the experiments. The heterogeneities were simulated by using powders heated at 1600 °C to isolate their specific dissolution behaviour. The sintered powders surrogates dissolved extremely slowly in solution. However, the normalized dissolution rates increased when HNO_2 catalytic species were introduced in the solution. Another set of experiments obtained by varying the incorporation rates in heterogeneities showed a decrease of the dissolution rate with increasing incorporation rate of Th-enriched heterogeneities. This effect is counterintuitive as Th-enriched heterogeneities are not supposed to dissolve during the first instants of the dissolution. Microscopic study based on *operando* monitoring of the solid/liquid interface highlighted preferential dissolution zones with a dissolution front in the matrix and the refractory character of the heterogeneities. Finally, the collected residues of dissolution were also characterized. They showed slight dissolution progress with the formation of dissolution pits, preferential attacks of the grain boundaries and a mechanism resembling the cracking core model of dissolution. This work offers a first study of the dissolution of heterogeneous $U_{1-x}Th_xO_2$ mixed oxides with a matrix-inclusion type microstructure.

Highlights:

- Polished heterogeneous $U_{1-x}Th_xO_2$ pellets have been prepared, characterized then submitted to dissolution tests in nitric acid solutions.
- Different behaviours during dissolution have been observed between embedding U-enriched phase and Th-enriched heterogeneities.
- Increasing the quantity of heterogeneities in the pellets led to the decrease of the dissolution rates.
- $U_{1-x}Th_xO_2$ sintered powders with $x > 0.58$ dissolved slowly in the absence of HNO_2 catalytic species.

1. Introduction

The dissolution of spent nuclear fuel is a key step to manage front-end of the nuclear fuel cycle at the industrial scale, especially in the case of plutonium-bearing mixed oxides (MOX) fuels dedicated to Sodium Fast Reactors (SFR). Indeed, plutonium concentration has been shown to greatly affect the kinetics of dissolution of $U_{1-x}Pu_xO_2$ fuels due to the refractory nature of plutonium [1]. Vollath *et al*. [2] showed that the solubility of $U_{1-x}Pu_xO_2$ in concentrated boiling nitric acid drastically decreased from x = 0.35 until being refractory to dissolution. This phenomenon, believed to originate from a crystal structure change [3] of the solid solution from these concentrations, is of importance since future SFR MOX fuels should contain up to 30 mol.% of plutonium and prove challenging to dissolve completely [4]. Research on recycling SFR MOX fuels is of importance as a reactor fleet comprising of SFR only would be able to run entirely on legacy stock of depleted uranium, eliminating the need to mine uranium [5]. Moreover, recent studies have shown that an intermediate fleet of PWRs and up to 30% SFRs would prove able to enhance plutonium economy and stabilize plutonium inventories [6].

An important property of MOX fuels, especially those showing high contents of plutonium, concerns their cationic heterogeneity at the microscopic scale, i.e., the presence of plutonium-enriched local agglomerates. The heterogeneity of such fuels has been shown to affect several of their thermal properties [7], release of fission gases during irradiation [8] or resistance to the formation of hotspots [9]. That explains why it has been studied extensively in the literature. However, an often-overlooked aspect of the presence of cationic heterogeneities in the SFR MOX fuels is their impact on the dissolution behaviour. Indeed, as plutonium content in such fuels is higher, they dissolve more slowly while plutonium enriched agglomerates are known to participate significantly in the final balance of residues of dissolution [10,11] which could induce significant risks in terms of criticality [12].

Then, a precise study of these cationic heterogeneities may be of importance to assess their dissolution kinetics. Yet, most dissolution studies in the literature disregard their influence [2,12–14] or are performed on homogeneous solid solutions synthesized by coprecipitation routes [14].

Since plutonium is a high specific activity radioelement, thorium has been broadly preferred as a simplified surrogate for the dissolution of plutonium-based oxides [15–18]. Desigan *et al.* [19] gave four criteria of importance when choosing a suitable surrogate element for the study of the solution chemistry of any chemical species. These criteria are (i) the stable oxidation state of the species, (ii) the respective ionic radii of the stable species, (iii) the leaching behaviour of these ionic species and (iv) the electrochemical parameters of the chemical species under investigation. Despite being only stable in the +IV oxidation state in solution [20], the non-oxidative dissolution of ThO_2 in nitric acid followed a similar complexation-based mechanism than PuO_2 [21,22] in acid media (eq. (1)) and is equally kinetically unfavourable :

$$AnO_2 + 4\,H^+ \rightarrow An^{4+} + 2\,H_2O \quad (1)$$

(An = Pu, Th)

$U_xTh_{1-x}O_2$ mixed oxides exhibit a significant decrease of the dissolution rate for Th mole loading higher than 0.6 [23]. It differed slightly from $U_{1-x}Pu_xO_2$ mixed oxides whose dissolution is exhibiting the same phenomenon for $x \geq 0.4$ [2]. Previous work from Claparede *et al.* [18] dealing with the dissolution of $U_{0.5}Th_{0.5}O_2$ heterogeneous oxides synthesized by mechanically grinding of pure UO_2 and ThO_2 mixtures prior to the sintering step showed different behaviour from the U-rich and Th-rich phases at the microscopic scale. However, this study only focused on the early beginning of the dissolution behaviour

and disregarded the influence of the presence of heterogeneities regarding to the formation of dissolution residues. Furthermore, the equimolar mixing of UO_2 and ThO_2 was not associated to the formation of the matrix-inclusions type microstructure representative of the spatial distribution of cationic heterogeneities in SFR MOX fuels.

The focus of this work is thus to study the dissolution behaviour of heterogeneous $U_{1-x}Th_xO_2$ mixed oxides in various nitric media with a focus on the role of thorium-rich cationic heterogeneities in both the dissolution behaviour of the oxide and the presence of undissolved residues. The cationic heterogeneity will be obtained by mixing $U_{1-x}Th_xO_2$ homogeneous powders prepared from co-precipitation techniques and the powders will be separated in two groups. The first group of solid solutions, which will be later labelled as the "matrix" phase, represents soluble phase in which thorium concentration is significantly lower than the solubility gap. The second group of solid solutions, later called as "heterogeneities", will contain enough thorium loading to become refractory. Finally, the "heterogeneities" will be composed of two populations of $U_{1-x}Th_xO_2$ powders with x = 0.6 and 0.8 in order to investigate the behaviour of heterogeneities with a thorium concentration right before and after the solubility rate gap.

2. Theory

Dissolution of $U_{1-x}Th_xO_2$ mixed oxides is known to balance between that of both uranium and thorium oxides depending on the stoichiometry of the oxide [17]. Inoue [24] proposed the mechanism presented in Eq. (2) to describe the oxidative dissolution of UO_2 in nitric medium. The nitrogen dioxide can thus disproportionate to form HNO_2, which can react with UO_2 as proposed in Eq. (3). The possibility for HNO_2 to be regenerated from NO and NO_2 recombination [25], as expressed in Eq. (4), makes the general mechanism as autocatalytic [26,27]. Eq. (4) being a chemical equilibrium, the increased concentration of HNO_2 due to the dissolution of UO_2 tends to return to the concentration of dynamic equilibrium if the production of HNO_2 ends.

$$UO_2(s) + 2\ NO_3^-(aq) + 4\ H^+ \rightarrow UO_2^{2+}(aq) + 2\ NO_2(aq) + 2\ H_2O \quad (2)$$

$$UO_2(s) + 2\ HNO_2(aq) + 2\ H^+ \rightarrow UO_2^{2+}(aq) + 2\ NO(aq) + 2\ H_2O \quad (3)$$

$$NO + NO_2 + H_2O \rightleftharpoons 2\ HNO_2 \quad (4)$$

Dalger *et al.* [15] and others [28–30] described the dissolution of these systems by a 4-step sequence. The first step represents an initial rapid release of very small mass of solid (≈ 0.05 wt.%) that could arise from the dissolution of poorly crystallized small particles or secondary phases. The second step (up to ≈ 0.6 wt.%) is a slow linear phase of non-catalyzed dissolution resulting in the build-up of catalytic species. The third step is triggered when enough catalytic species have been accumulated in solution or at the solid/solution interface and the catalysis begins, resulting in a period of accelerating dissolution rate due to both a rapid increase in the concentration of catalytic species and a dramatic increase of the reactive surface of the solid [31]. Finally, for a progress of 40-60 wt.%, the dissolution rate decreases until entering a slower trailing period as there is not much reagent left, leading to a decrease of the reactive surface area [30].

3. Experimental

3.1. Samples preparation

All heterogeneous $U_{1-x}Th_xO_2$ mixed oxide powders were synthesized by wet chemistry route involving hydroxide precipitation [32]. The thorium chloride solution serving as precursor was prepared by dissolving thorium nitrate pentahydrate (Sigma Aldrich, 99%) in 4 mol.L^{-1} HCl solution. The solution, contained in glass, was evaporated in a sand bath to dryness then rehydrated with the same 4 mol.L^{-1} HCl solution three times to eliminate nitrate ions from the solution. The uranium chloride solution was prepared by dissolving uranium metal chips in 6 mol.L^{-1} HCl solution before being concentrated by heating under reflux in a glass flask [33]. The resulting stock solutions were analyzed by ICP-AES to perform the hydroxide synthesis. After mixing the uranium and thorium chloride solutions, the mixtures were then poured at room temperature under active stirring in a 4 mol.L^{-1} NH_3 solution, with an excess of ammonia of 400 mol.%. After 30 minutes, the precipitates were washed twice with deionized water and once with ethanol and separated from the supernatants by centrifugation (5 min, 4500 rpm). The obtained uranium(IV)-thorium hydroxide powders were finally calcined during 4 hours under a reducing atmosphere (Ar – 4% H_2). The temperature of the thermal treatment ranged from 800 °C to 1200 °C depending on the expected use of the powder. Indeed, for thorium enriched agglomerates, higher treatment temperature was chosen to reduce the specific surface area of the powders and thus their reactivity during the sintering step. By this way, thermal diffusion and homogenization during sintering was reduced, leading to poor integration of Th-rich agglomerates in the U-rich matrix. However, a too high temperature could induce a too low sinterability, resulting in the presence of remaining porosity around the Th-enriched agglomerates. A good compromise has been obtained by heating the embedding "matrix" (i.e., $U_{0.7}Th_{0.3}O_2$) at 800 °C and the Th-enriched "heterogeneities" at 1200 °C ($U_{0.4}Th_{0.6}O_2$ and $U_{0.2}Th_{0.8}O_2$).

The reactive surface areas of the $U_{1-x}Th_xO_2$ powders were determined by N_2 adsorption using the BET method (Micrometrics - ASAP 2020). The powders were also characterized by Powder X-Ray Diffraction (PXRD), by collecting the XRD patterns between 5° and 100° (2θ) using a Bruker D8 Advance X-ray diffractometer (Cu $K\alpha_{1,2}$ radiation, λ = 1.5418 Å) with a 0.02° step and a measuring time of 2 s per step.

The various mixed oxide powders were characterized before and after heating. Table 1 shows the precipitation yields obtained for the different $U_{1-x}Th_xO_2$ powders after analyzing the supernatant by ICP-OES. Actinide concentrations determined in the supernatants were lower than the detection limits (i.e. 0.1 ppm). Thus, the starting precipitation was found to be quantitative. Additionally, the stoichiometry measured from X-EDS and after total dissolution of the heated powders confirmed the previous results. The measured specific surface area values decreased according to the increase of the heating temperature, eventually reducing the sinterability of the powders calcined at 1200 °C.

Table 1

Expected stoichiometry, heating temperature, specific surface area, precipitation yields, unit cell parameters as well as stoichiometry determined by X-EDS and ICP-OES for the heated mixed oxides.

Expected stoichiometry	Heating temperature (°C)	S_{SA} ($m^2.g^{-1}$)	Precipitation yield (U & Th)	Th/(U+Th) from X-EDS	Th/(U+Th) from dissolution	a (Å)
$U_{0.7}Th_{0.3}O_2$	800	30.6 ± 0.2	> 99.8 %*	0.29 ± 0.01	0.28 ± 0.01	5.4978(3)
$U_{0.4}Th_{0.6}O_2$	1200	15.8 ± 0.1	> 99.7 %*	0.60 ± 0.01	0.59 ± 0.03	5.5439(6)
$U_{0.2}Th_{0.8}O_2$	1200	11.0 ± 0.1	> 99.6 %*	0.80 ± 0.01	0.78 ± 0.04	5.5699(5)

*Elemental concentrations in the supernatant were lower than the detection limit so yields reflect the minimum value of the precipitation yield when elemental concentration are equal to the detection limit.

The PXRD patterns of all the prepared $U_{1-x}Th_xO_2$ powders are presented in Fig. 1a for several *x* values. They were refined using the Rietveld method considering the fluorite type structure (Fm3m) characteristic of pure UO_2 (JCPDS files 01-081-0792) and ThO_2 (JCPDS files 00-042-1462). The determined unit cell parameter obtained for the three powders are given in Table 1 and shown in Fig. 1b along with values from Xiao *et al.* [34] calculated at 25 °C for UO_2 and ThO_2. The obtained values are in good agreement with that reported in the literature and follow the Vegard's law characteristic of the $U_{1-x}Th_xO_2$ solid solutions. However, the $U_{0.72}Th_{0.28}O_2$ powder slightly deviates from the Vegard's law, which has been previously reported by Balice *et al.* [35] and Trzebiatowski *et al.* [36]. These values were later used to calculate the "theoretical" density of the heterogeneous pellets. It is worth noting that the $U_{0.72}Th_{0.28}O_2$ sample heated at 800 °C appeared to be less crystallized compared to all samples heated at 1200 °C. These powders were further used to prepare dense pellets showing various heterogeneities.

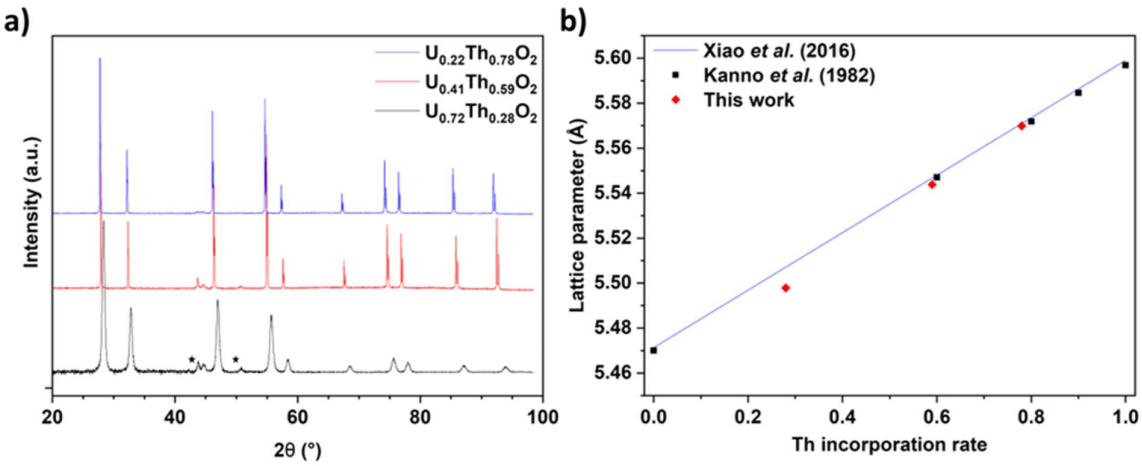

Fig. 1. (a) PXRD patterns of $U_{1-x}Th_xO_2$ oxides prepared with various x values (T = 800 °C for x = 0.28 and 1200 °C for x = 0.59 and 0.78) and (b) associated lattice parameter determined with the Rietveld method compared to data from Kanno *et al.* [37] and calculated Vegard's Law at 25 °C from Xiao *et al.* [34]. ★ Refers to the peaks of the sample holder.

Dense pellets were prepared from powdered mixtures with various U and Th stoichiometries ($U_{0.72}Th_{0.28}O_2$ for the matrix, $U_{0.41}Th_{0.59}O_2$ and $U_{0.22}Th_{0.78}O_2$ for the heterogeneous phases) which were each manually ground to deagglomerate the powders. An overview of the relative rate of the different powders for all the samples prepared during this study is given in Table 2. The resulting blend was then pressed uniaxially at 500 MPa with a 5 mm of diameter a tri-shell die. After 30 min of air sweeping, the green pellets were finally sintered in an alumina crucible at 1600 °C during 4 hours under reductive

atmosphere (Ar – H_2 4%) to avoid any oxidation of uranium (IV) during the heating step. Once obtained, the dense pellets were polished on both faces in three steps (10 µm, 5 µm and 1 µm) to ensure the absence of polluting species that could be restrained during the sintering step, to facilitate X-EDS studies and offer an in-depth point of view for the characterization of the heterogeneities. A schematic representation of the methodology used to prepare and characterize the samples is given in Fig. 2.

Table 2
Average stoichiometry, mass and relative share of the different powders making up the mixture of the pellets sintered at 1600 °C for this study.

Sample	Average Stoichiometry	Mass (mg)	$U_{0.72}Th_{0.28}O_2$ (mol.%)	$U_{0.41}Th_{0.59}O_2$ (mol.%)	$U_{0.22}Th_{0.78}O_2$ (mol.%)
Pe1*	$U_{0.68}Th_{0.32}O_2$	170.2 ± 0.1	89.6 ± 0.2	5.2 ± 0.1	5.2 ± 0.1
Pe2	$U_{0.72}Th_{0.28}O_2$	155.3 ± 0.1	100	-	-
Pe3	$U_{0.69}Th_{0.31}O_2$	132.1 ± 0.1	94.8 ± 0.1	-	5.2 ± 0.1
Pe4	$U_{0.67}Th_{0.33}O_2$	138.5 ± 0.1	89.7 ± 0.2	-	10.3 ± 0.2
Pe5	$U_{0.64}Th_{0.36}O_2$	141.8 ± 0.1	84.7 ± 0.3	-	15.3 ± 0.3
Pe6	$U_{0.62}Th_{0.38}O_2$	132.8 ± 0.1	79.2 ± 0.4	-	20.8 ± 0.4
Pe7	$U_{0.60}Th_{0.40}O_2$	135.9 ± 0.1	75.0 ± 0.5	-	25.0 ± 0.5

* Representative pellet of the Pe1 series among the panel of synthesised pellets

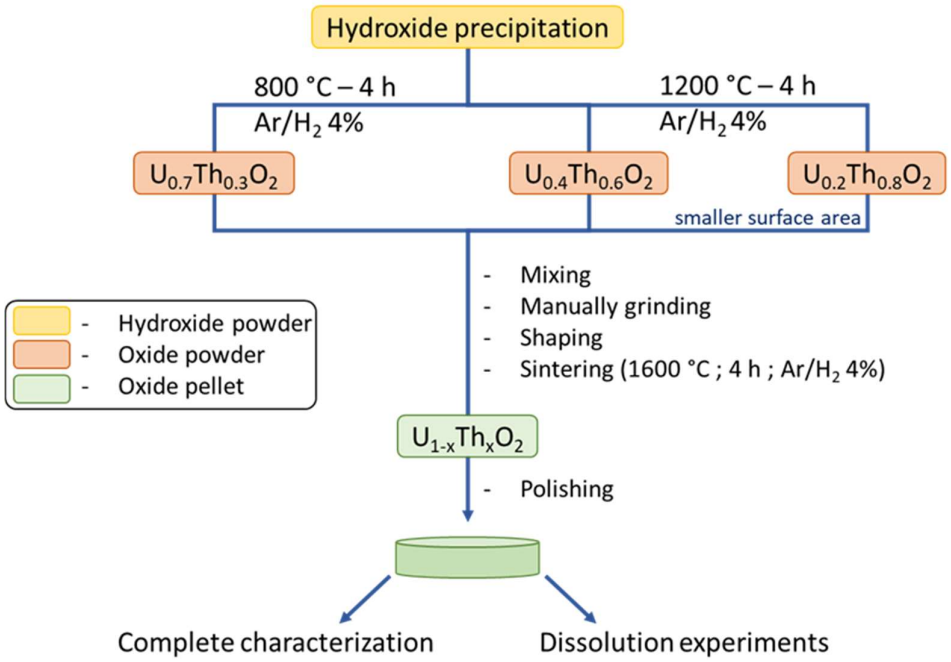

Fig 2. Schematic representation of the methodology used to prepare polished heterogeneous mixed oxide samples.

3.2. Pellets characterization

The densification rates of the sintered and polished pellets were determined using an electronic calliper to make geometric measurements and by helium pycnometry (Micrometrics – AccuPyc II 1340). As it was difficult to determine a "theoretical" density for heterogeneous oxides due to local stoichiometry variations, the obtained densities were compared to a calculated density considering the average stoichiometry of the oxide (i.e., equivalent to that of an homogeneous material with average stoichiometry). This approach was considered to be valid here since uranium-thorium dioxides

formed solid solution whose "theoretical" density followed the Vegard's law [23]. The comparison of both values obtained from geometric determinations, d_{geo}, and by He pycnometry, d_{pycno}, with the "theoretical" density, d_{th}, led us to determine the total (P_{tot}), closed (P_{closed}) and open (P_{open}) porosities, as follows (equations (5), (6) and (7)):

$$P_{tot} = 1 - \frac{d_{geo}}{d_{th}} \quad (5)$$

$$P_{closed} = 1 - \frac{d_{pycno}}{d_{th}} \quad (6)$$

$$P_{open} = P_{tot} - P_{closed} \quad (7)$$

The morphological characterization of both powders and pellets was performed by Scanning Electron Microscopy (SEM) with a FEI Quanta 200 environmental apparatus using alternatively a Back-Scattered Electron Detector (BSE) or a Secondary Electron Detector (SE) in vacuum conditions with an acceleration voltage of 15 kV. Since neither experiments on powders nor on sintered pellets required a metallization step, characterizations by SEM were not destructive.

Specific surface area of the dense pellets (S_{SA}, in $m^2.g^{-1}$) were too low to be determined by BET method. Therefore, these values were evaluated by image analysis , using the SESAM method (Study of Evolving Surface Area by Microscopy) from SEM micrographs of the sintered pellets, as reported by Horlait *et al.* [38] and Dalger *et al.* [15]. It was calculated by adding the geometric surface area (often negligible) and that coming from open porosity; this latter being obtained by thresholding SEM micrographs to discriminate the grains (white) from the open pores (black). The open pores were treated as cylindrical in shape to calculate their radius and interior surface. The resulting S_{SA} consisted in an average value from 12 micrographs acquired at low magnification (× 1000, i.e. 126 µm × 110 µm), which was considered to be representative of the whole material.

The local stoichiometry of the polished pellets was determined by X-ray Energy Dispersive Spectroscopy (X-EDS). X-EDS spectra were recorded on non-metallized samples at low magnification (× 400, i.e. 360 µm × 270 µm) in vacuum conditions at a working distance of 10.5 mm under an acceleration voltage of 15 kV, creating a 30 kcps photon flux on the detector. An automatic 4 × 4 cartography of the samples was performed with an overlapping of 10 % between each image before generating a mosaic using the MosaicJ plugin from the imageJ software [39]. The obtained large quantitative maps (up to 1.33 mm × 1mm) allowed to develop statistical study of the cationic heterogeneities.

3.3. Dissolution experiments

Dissolution tests were performed under static conditions (without stirring) in polytetrafluoroethylene vessels at 60 °C or 90 °C in 25 mL of nitric acid with various concentrations (2 and 4 $mol.L^{-1}$) prepared from analytical grade reagents (Sigma Aldrich, 99%). The 130 to 170 mg pellets were cut in half. One piece was placed in the reactor for days to months depending on the apparent progress of the reaction. Aliquots of 0.2-2 mL of the leachate were regularly taken off then renewed with fresh solution. After centrifugation (5 min, 5000 rpm), they were finally diluted in 0.2 $mol.L^{-1}$ nitric acid prior the determination of the elemental concentrations in the solution.

Elemental concentrations were monitored through ICP-OES measurements (iCAP 7000 Plus Series ICP-OES) with selected wavelength for uranium (λ = 263.553 nm, 385.958 nm and 409.014 nm) and thorium (λ = 283.231 nm and 401.913 nm) in order to avoid any interference between the studied elements.

The precise concentrations were determined using standard solutions prepared by dilution of Th and U from certified solutions (PlasmaCAL, single element calibration standards for ICP-OES, SCP Science) of 1000 mg.L^{-1} in 0.2 mol.L^{-1} nitric acid. The elemental concentrations were determined from three replicates and the considered relative uncertainty (usually around 3-4 %) were considered as two times the standard deviation of the replicates. In these conditions, the detection limit of the elements reached 0.1 ppm.

The relative mass of dissolved element, $\Delta m_i/m_{i,0}$ (%) was obtained from equation (8):

$$\Delta m_i(t)/m_{i,0} = \frac{C_i(t) \times V}{f_i \times m_0} \times 100 \quad (8)$$

Where $m_i(t)$ (g) is the dissolved mass of the element at time t, calculated from the elemental concentration $C_i(t)$ (g.L^{-1}) (i = U or Th) and V (L) the volume of solution, and $m_{i,0}$ is the initial mass of the element i, calculated from f_i the mass fraction of the element i and m_0 (g) the initial mass of the solid.

The normalized weight loss, $N_L(i)$ (g.m^{-2}) can be calculated after normalization by the reactive surface area, $m_0 \times S_{SA}$, and by the mass ratio, f_i, of the element measured in the leachate, using the following equation:

$$N_L(i) = \frac{m_i}{f_i \times S_{SA} \times m_0} \quad (9)$$

Consequently, the normalized dissolution rate $R_L(i)$ (g.m^{-2}.d^{-1}) is defined as the derivative of the normalized weight loss $N_L(i)$ over time, as follows (eq. 10):

$$R_L(i,t) = \frac{d\, N_L(i,t)}{d\, t} \quad (10)$$

Dissolution tests described above were performed to provide a general information on the dissolution of the $U_{1-x}Th_xO_2$ heterogeneous pellets at the macroscopic level. However, the dissolution of crystalline materials is generally considered to be an heterogeneous phenomenon [40] with preferential dissolution zones such as pores, cracks and grain boundaries [30,41,42], as described by Claparede *et al*. [18]. This also justified to investigate the dissolution of such sintered heterogeneous pellets at the microscopic scale with the help of *operando* monitoring of the solid/solution interface. This consisted in the repetition of dissolution steps in nitric acid media followed by observations with the help of environmental scanning electron microscopy (ESEM) according to the methodology already described by Cordara *et al.* [43]. ESEM observations were repeated in the same zones of the materials and magnifications after each dissolution step. The successive images were then stacked together to build a “movie” of the dissolution progress.

4. Results

4.1. Samples characterization

The geometric and pycnometric densities obtained for the synthetized pellets are reported in Table 3, which allowed evaluating the open and close porosities following from Eq. (5), (6) and (7). Each ranged from 1 to 5 %. Specific surface areas obtained from the SESAM method on the FiJi software are also gathered in Table 3. At least twelve SEM micrographs, considered to be representative of the whole pellet, were used to determine the S_{SA} for all the pellets. As expected, the obtained values, ranging from 3.2×10^{-3} to 1.1×10^{-2} $m^2.g^{-1}$, were two to three orders of magnitude higher than the geometric values (around 2×10^{-4} $m^2.g^{-1}$) and too low to be determined by BET method even using Kr adsorption. The uncertainty associated to S_{SA} values was two times the standard deviation determined from the set of images used for this method. All the prepared pellets were well sintered, with geometric density and pycnometric density in the range of 93-96 % and of 95-97 %, respectively (Table 3) while the obtained S_{SA} values were typically an order of magnitude lower than those described by Dalger *et al.* [15,44] for $U_{0.75}Th_{0.25}O_2$ homogeneous unpolished mixed oxides obtained from oxalate precursors.

Table 3. Geometric and He-pycnometric densities as well as open and closed porosities measured on sintered pellets and associated specific surface area (S_{SA}) determined by the SESAM method.

Sample	$\frac{d_{geo}}{d_{th}}$ (%)	$\frac{d_{pycno}}{d_{th}}$ (%)	P_{Closed} (%)	P_{Open} (%)	S_{SA} ($m^2.g^{-1}$)
Pe1	96 ± 2	97 ± 2	3 ± 2	1 ± 1	(3.2 ± 0.2) x 10^{-3}
Pe2	94 ± 2	95 ± 2	5 ± 2	1 ± 1	(5.5 ± 0.2) x 10^{-3}
Pe3	95 ± 2	96 ± 2	4 ± 2	1 ± 1	(5.1 ± 0.3) x 10^{-3}
Pe4	96 ± 2	97 ± 2	3 ± 2	1 ± 1	(3.5 ± 0.2) x 10^{-3}
Pe5	94 ± 2	96 ± 2	4 ± 2	2 ± 2	(5.2 ± 0.7) x 10^{-3}
Pe6	94 ± 2	97 ± 2	3 ± 2	3 ± 2	(6.7 ± 0.2) x 10^{-3}
Pe7	93 ± 2	97 ± 2	3 ± 2	4 ± 2	(1.1 ± 0.1) x 10^{-2}

A SEM micrograph of a dense polished pellet containing 10.4 mol.% of heterogeneities (Pe1) is presented in Fig. 3a. One can observe the presence of small, roundish pores characteristic of such dense pellets. The image analysis of the unpolished pellets gave an average grain size of 7.1 ± 0.7 µm, which value is comparable to that obtained for $U_{1-x}Th_xO_2$ pellets synthesized from oxalate precipitates and sintered at 1500 °C (5-10 µm) [18]. Furthermore, Fig. 3b shows an example of a 4 × 4 mosaic of X-EDS micrographs of Pe1 reconstructed using the MosaicJ plugin. The two populations of heterogeneities: $U_{0.41}Th_{0.59}O_2$ (in yellow) and $U_{0.22}Th_{0.78}O_2$ (in red) are clearly discernible from the embedding matrix $U_{0.41}Th_{0.59}O_2$ (in blue). The reconstruction technique produces high-resolution (around 11 $Mpx.mm^{-2}$) micrographs of large surfaces (up to 1.3 mm^2) allowing for a reliable characterization and statistical analysis of the heterogeneities.

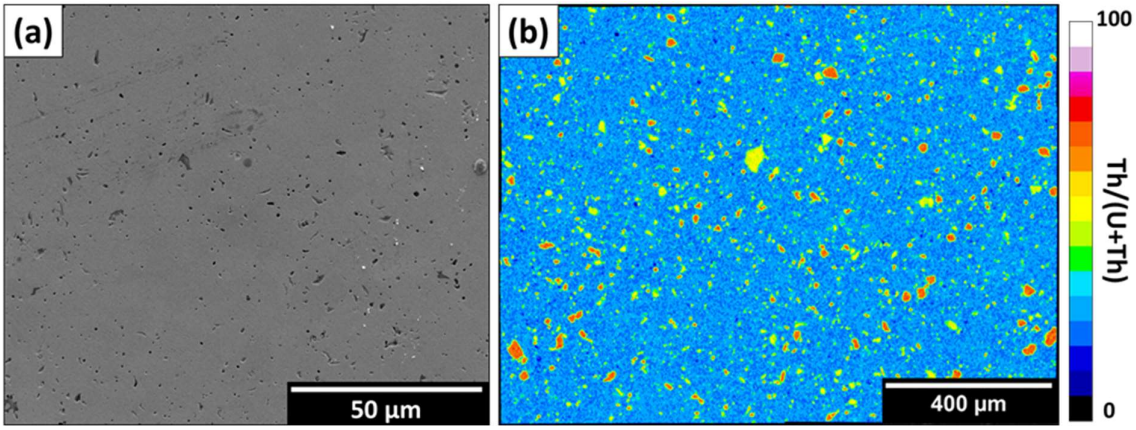

Fig 3. (a) SEM micrograph of the sintered and polished pellet Pe1 and (b) 4 × 4 mosaic of X-EDS micrographs for Pe1 showing the spatial distribution of Th-enriched heterogeneities. For interpretation of the references to colour in this figure, the reader is referred to the web version of this article.

To simplify the system and with the goal of studying the specific impact of the incorporation rate of heterogeneities on the overall dissolution rate, a series of pellets were synthesized with only two powders populations, i.e., $U_{0.72}Th_{0.28}O_2$ for the matrix and $U_{0.22}Th_{0.78}O_2$ for heterogeneities. 4 × 4 mosaics of X-EDS micrographs for the pellets obtained with heterogeneities incorporation rates of 5.2 mol.%, 10.3 mol.%, 15.3 mol.%, 20.8 mol.% and 25.0 mol.% are gathered in Fig. 4a, 4b, 4c, 4d and 4e, respectively. Fig. 4f shows the number of particles bigger than a given equivalent circle diameter (ECD – defined as the diameter of a circle of the same area) per mm² as well as the cumulative surface occupied by all particles smaller than a given ECD. The obtained mosaics were studied through image analysis, as reported in Table 4. This table underlines the effect of the increase of the heterogeneities incorporation rate on the presence of observed particles and their size distribution and occupied surface.

The SEM micrographs in Fig. 3a show a well-sintered pellet with small open porosity in agreement with density values obtained in Table 3. The 4 × 4 X-EDS mosaic in Fig. 4b shows the advantages of using a stitching technique to study such materials. Indeed, stitching multiple X-EDS cartographies allowed for characterizing a large surface while keeping a small pixel size allowed for high-resolution images recording.

If the mosaic is representative of the mixture, then the observed surface occupied by heterogeneities should be equal to the content of the Th-rich powders in the mixture. The observed surface occupied by the heterogeneities (Table 4) was always in agreement with the expected content and thus close to the expected surface (within 10 % of relative difference), validating the general process to prepare heterogeneous pellets. The differences between the expected and obtained surface of the particles was mainly explained by three phenomena, namely the inherent statistical variation of a localized measurement, the interacting volume of the SEM and the thermal diffusion of elements during the sintering step. The statistical variation, which can overestimate or underestimate the measured value, is minimized due to the large size of the mosaics (approx. 9-10% of a face of the pellet).

In Fig. 4, thorium enriched heterogeneities are angular and cover a range of equivalent circle diameters (ECD - defined as the diameter of a circle of the same area) from 1 µm (limited by the electron beam – matter volume interaction) to more than 100 µm. The density of particles per mm² typically increased with the heterogeneities loading in the pellet as shown in Table 4. For all pellets, the number of particles larger than a given ECD rapidly decreased but the larger particles accounted for a significant fraction of the surface occupied by heterogeneities. Particles larger than 30 µm represented only a small fraction in number but occupied a large part of the surface. They represented 0.8 % of the particles for the pellet containing 5.2 mol.% of heterogeneities but occupy 15.5 % of the surface of the thorium enriched phase. For the pellet containing 25.0 mol.% of heterogeneities, they represented about 2.1 % in number and 30.8 % of the occupied surface. This effect may arise from the increased density of particles leading to some particles fusing together and being analyzed as a larger one during the segmentation step of the image analysis. In the opposite way, small particles with an ECD smaller than 10 µm represented a large contribution of the particles in numbers (typically around 79-86 % of the particles) but a smaller contribution of the surface occupied by the heterogeneities (typically around 17-28 % of the occupied surface).

The slower slope obtained in Fig. 4f (right) in the presence of higher content of heterogeneities tends to confirm this trend. Indeed, the pellet containing 20.8 mol.% of heterogeneities showed a high number of particles per mm², a low number of large particles (ECD > 30 µm) and a reduced contribution of large particles in the occupied surface. The specific behaviour of the pellet showing 20.8 mol.% of heterogeneities could come from some differences during the grinding step leading to different particle-size distribution.

Table 4. Observed and expected surface occupied by the $U_{0.22}Th_{0.78}O_2$ heterogeneities, density of the particles per mm² and contribution of particles greater than 30 µm in the occupied surface of heterogeneities for the prepared sintered pellets.

Sample	Heterogeneities (mol.%)	Observed surface (%)	Observed/ Expected	Particles/ mm²	ECD<10µm (%)	$S_{<10µm}$ / S_{heter} (%)	ECD>30µm (%)	$S_{>30µm}$ / S_{heter} (%)
Pe1	10.4 ± 0.2	10.4 ± 0.1	1.00 ± 0.03	N. D.	N. D.	N. D.	N. D.	N. D.
Pe3	5.2 ± 0.1	5.45 ± 0.05	1.04 ± 0.03	924 ± 8	83.3	24.7	0.8	15.5
Pe4	10.3 ± 0.2	9.6 ± 0.1	0.93 ± 0.03	1360 ± 14	81.3	21.6	1.6	25.8
Pe5	15.3 ± 0.3	15.6 ± 0.1	1.02 ± 0.03	2300 ± 15	82.2	21.0	1.8	28.4
Pe6	20.8 ± 0.4	18.9 ± 0.1	0.91 ± 0.03	3600 ± 19	85.6	27.6	0.6	14.0
Pe7	25.0 ± 0.5	25.9 ± 0.2	1.04 ± 0.03	3240 ± 25	79.3	16.8	2.1	30.8

N.D. stands for Not Determined

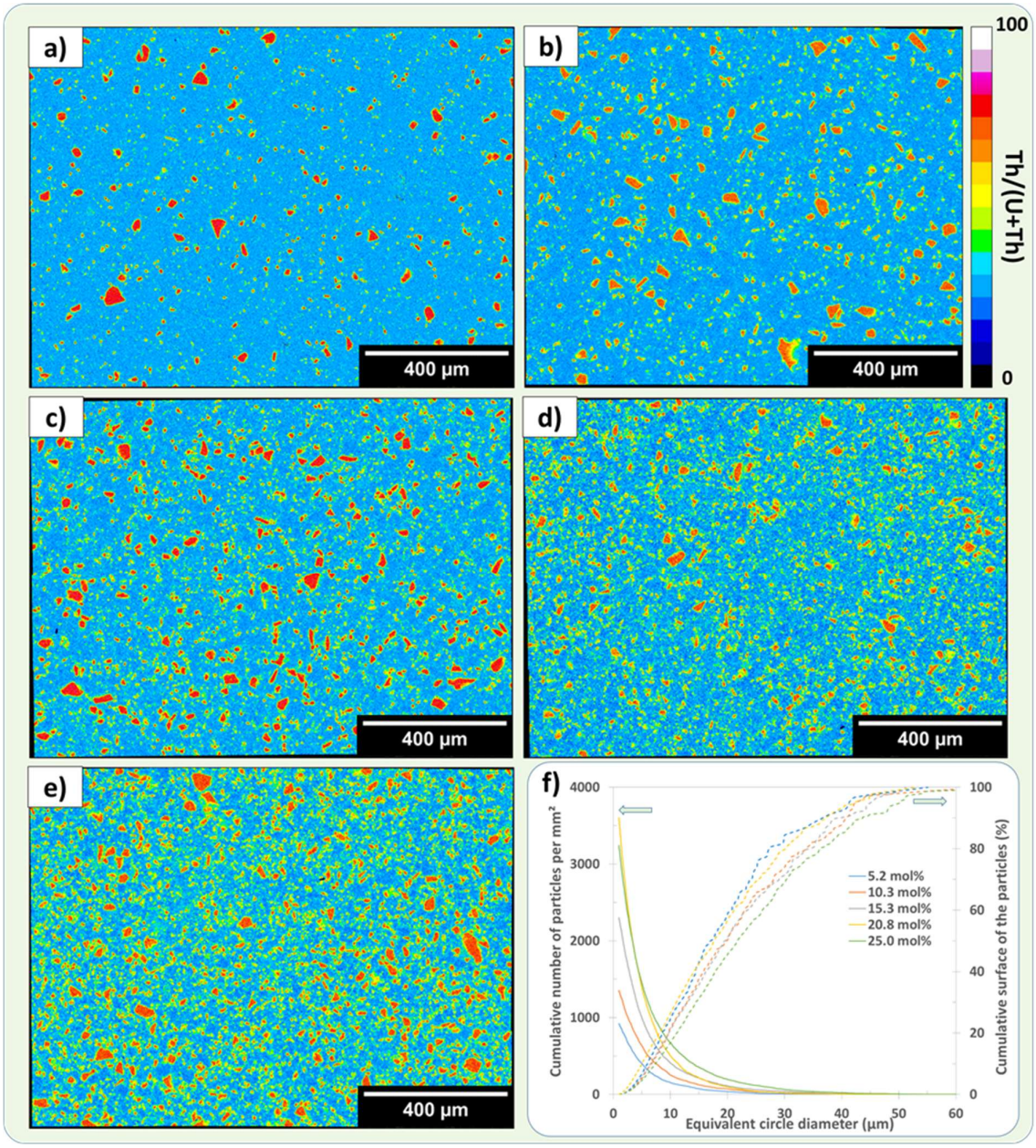

Fig. 4. X-EDS micrographs of heterogeneous $U_{1-x}Th_xO_2$ polished pellets containing (a) 5.2 mol.% of heterogeneities, (b) 10.3 mol.% of heterogeneities, (c) 15.3 mol.% of heterogeneities, (d) 20.8 mol.% of heterogeneities and (e) 25.0 mol.% of heterogeneities. (f) Cumulative number of particles per mm² and cumulative surface occupied by the particles versus their equivalent circle diameter (ECD). For interpretation of the references to colour in this figure, the reader is referred to the web version of this article.

4.2 Dissolution of homogeneous and heterogeneous $U_{1-x}Th_xO_2$ pellets

Dissolution curves obtained from U and Th releases for an homogeneous $U_{0.72}Th_{0.28}O_2$ pellet and an heterogeneous $U_{0.68}Th_{0.32}O_2$ pellet containing 10.4 mol.% of heterogeneities in 2 mol.L^{-1} HNO_3 at 60 °C are presented in Fig. 5. Curves in elemental concentration instead of relative dissolved mass for Fig. 5, Fig. 6, Fig. 7 and Fig. 9 are given as supplementary information if needed. In such aggressive conditions, the reaction was rapidly catalyzed, from the beginning for both experiments [30]. Therefore, only the steady state catalyzed regime (step 3 according to Dalger *et al.*), and the slower residual dissolution rate regime (step 4 according to Dalger *et al.*) were observed for all experiments [15]. The dissolution reaction being catalyzed from the beginning means that some change in the dissolution rate should come from an evolution of the reactive surface area when extending the dissolution time. The transition from the first to the second regime was observed when the dissolution rate started to decrease after reaching its maximum. Dissolution rates (expressed in wt.%.d^{-1}) associated to the steady state catalyzed regime correspond to the initial dissolution rates. The dissolution rates associated to the second regime referred to the residual linear trailing period observed for all the dissolution experiments. Both types of dissolution rates as well as the associated congruence ratios, defined as ratio of R_L(U) over R_L(Th), are gathered in Table 5.

The dissolution rate of the $U_{0.68}Th_{0.32}O_2$ pellet containing 10.4 mol.% of heterogeneities (Table 5) at the two observed steps is thus 2-3 times slower than that of the homogeneous pellet for both uranium and thorium while its specific surface S_{SA} is 1.7 times larger (at 5.5 x 10^{-3} vs 3.2 x 10^{-3} $m^2.g^{-1}$, respectively). Thus, the addition of 10.4 mol.% of Th-rich heterogeneities reduces the dissolution rate of the pellet.

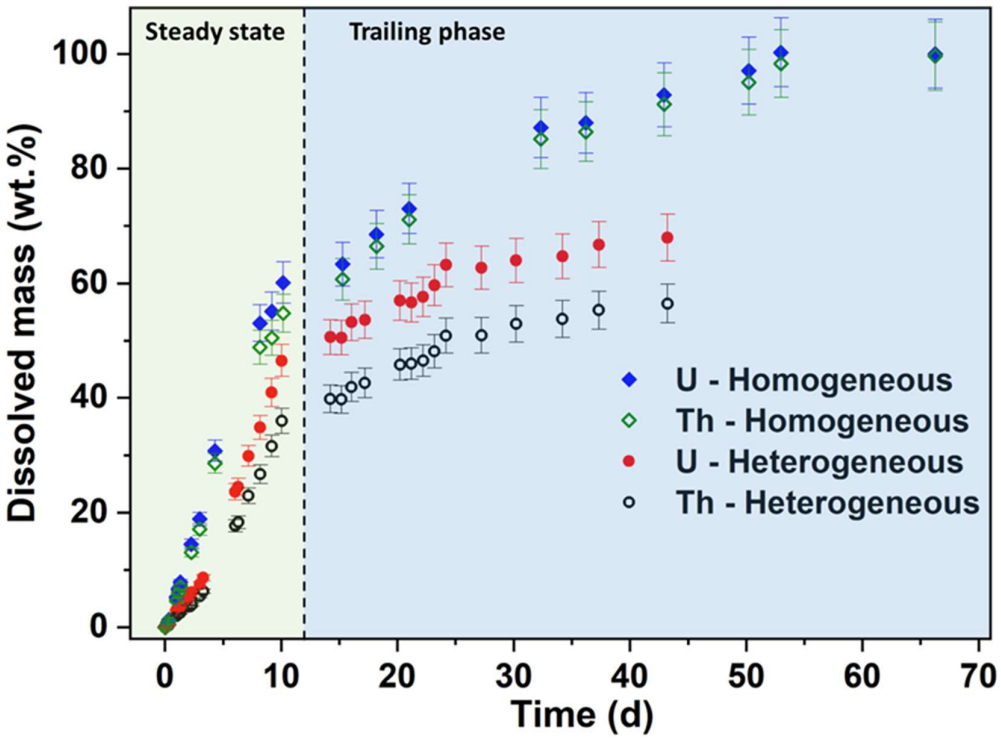

Fig. 5. Evolution of the dissolved mass of uranium and thorium during the dissolution of an homogeneous $U_{0.72}Th_{0.28}O_2$ pellet and an heterogeneous $U_{0.68}Th_{0.32}O_2$ containing 10.4 mol.% of heterogeneities at 60 °C in 2 mol.L^{-1} HNO_3. The steady state and trailing phase steps, as described by Dalger *et al.* [15], are outlined.

4.3 Effect of temperature and acidity

To emphasize the influence of the experimental conditions on the $U_{1-x}Th_xO_2$ heterogeneous mixed oxides dissolution, several $U_{0.68}Th_{0.32}O_2$ pellets containing 10.4 mol.% of heterogeneities were submitted to dissolution tests in 2 or 4 mol.L^{-1} HNO_3 at 60 °C (Fig. 6) or 90 °C (Fig. 7). Dissolution rates of the $U_{0.68}Th_{0.32}O_2$ heterogeneous pellets during the steady state catalyzed regime were found to be 2.6, 6.4, 25 and 51 wt.%.d^{-1} for uranium and 1.9, 4.8, 19 and 39 wt.%.d^{-1} for thorium at 60 °C and 2 mol.L^{-1} HNO_3, 60 °C and 4 mol.L^{-1} HNO_3, 90 °C and 2 mol.L^{-1} HNO_3, 90 °C and 4 mol.L^{-1} HNO_3, respectively. Moreover, the associated residual dissolution rates of heterogeneous pellets during the trailing phase (Table 5) reached 0.29, 0.61, 1.7 and 0.8 wt.%.d^{-1} for uranium and 0.32, 0.58, 1.6 and 0.9 wt.%.d^{-1} for thorium in the same sequence of dissolution conditions.

As expected, the dissolution rate increased with both acidity and temperature. Dissolution rates obtained during the catalyzed regime (Table 5) slightly increased when the concentration of nitric acid went from 2 to 4 mol.L^{-1} HNO_3 with a dissolution rate for both uranium and thorium multiplied by a factor of 2.5 at 60 °C and of 2 at 90 °C. Such a weak effect agreed well with that reported in literature [17,44]. The dissolution rates increased more sharply with the temperature. When increasing the temperature from 60 to 90 °C, the dissolution rates of both uranium and thorium rose by a ratio of 10 and 8 in 2 mol.L^{-1} HNO_3 and 4 mol.L^{-1} HNO_3, respectively (Table 5). Moreover, the effect of temperature was not only limited to kinetics. Indeed, experiments performed at 90 °C succeeded in reaching an almost full dissolution while experiments carried out at 60 °C remained partial and produced more residues at the end of the dissolution process. However, for all experiments, residues have been collected at the end of all dissolution tests then characterized.

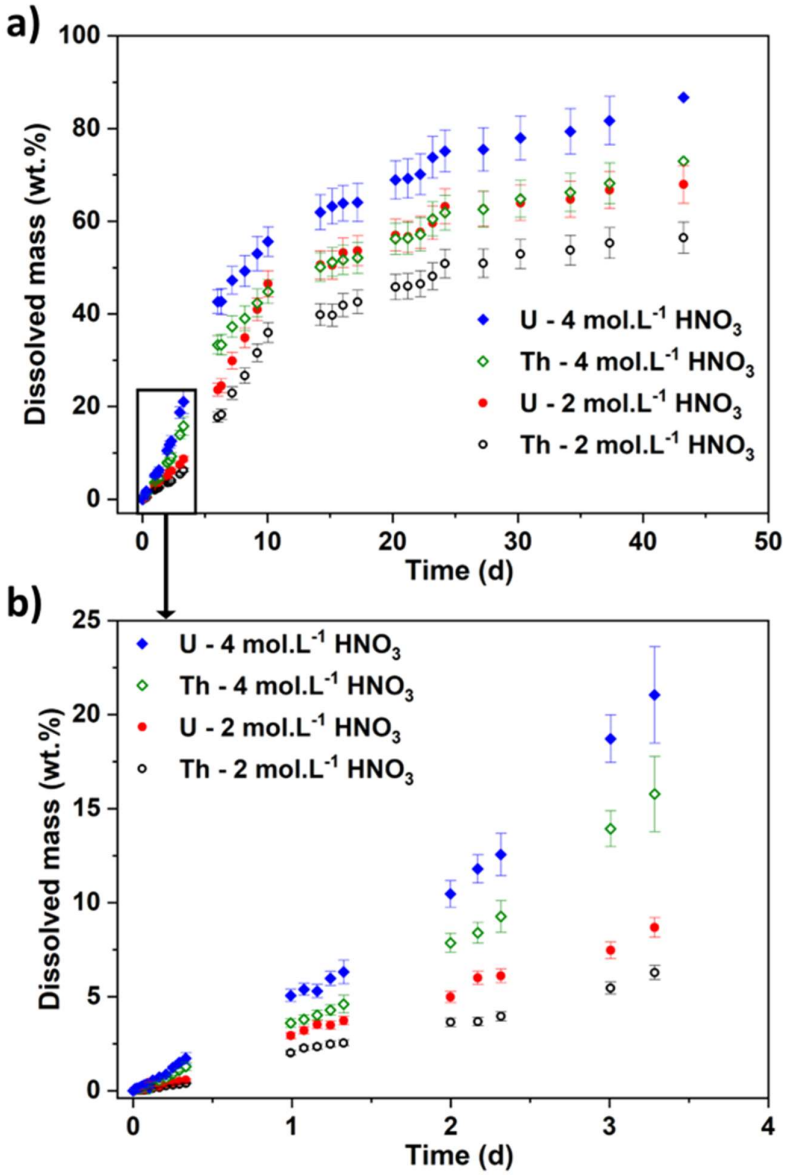

Fig. 6. (a) Evolution of the dissolved mass of uranium and thorium during the dissolution of heterogeneous $U_{0.68}Th_{0.32}O_2$ pellets containing 10.4 mol.% of heterogeneities in 2 and 4 mol.L^{-1} HNO_3 at 60 °C; (b) insert underlining the early stage of the dissolution.

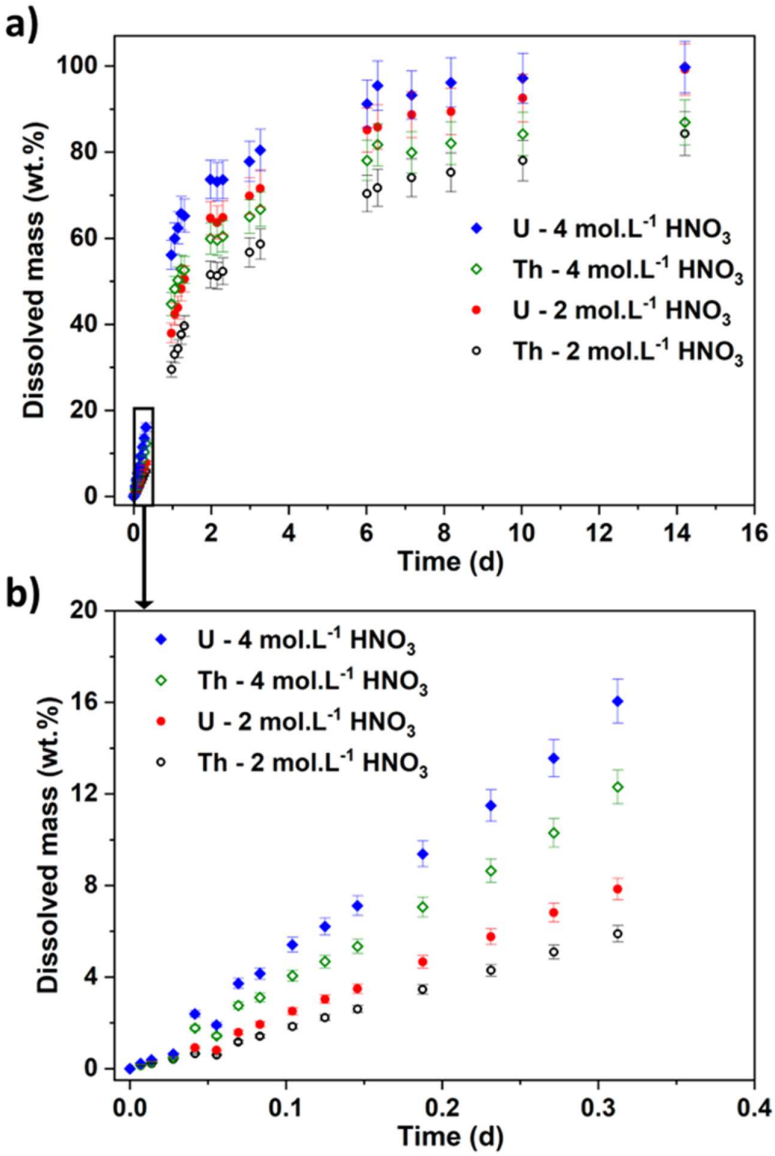

Fig. 7. (a) Evolution of the dissolved mass of uranium and thorium during the dissolution of heterogeneous $U_{0.68}Th_{0.32}O_2$ pellets containing 10.4 mol.% of heterogeneities in 2 and 4 mol.L^{-1} HNO_3 at 90 °C; (b) insert underlining the early stage of the dissolution.

Table 5. Dissolution rates determined from uranium and thorium releases in various experimental conditions during the two dissolution regimes as well as associated congruence ratio $r = R_L(U)/R_L(Th)$.

Step	T (°C)	C_{HNO3} (mol.L^{-1})	dm_U/dt (wt.%.d^{-1})	dm_{Th}/dt (wt.%.d^{-1})	r (U vs Th)
Steady state homogeneous	60	2	6.3 ± 0.3	5.7 ± 0.3	1.1 ± 0.1
Trailing phase homogeneous	60	2	1.0 ± 0.1	1.0 ± 0.1	1.0 ± 0.2
Steady state Heterogeneous	60	2	2.6 ± 0.2	1.9 ± 0.1	1.4 ± 0.2
	60	4	6.4 ± 0.4	4.8 ± 0.3	1.3 ± 0.2
	90	2	25 ± 1.5	19 ± 1.1	1.3 ± 0.2
	90	4	51 ± 3	39 ± 2.4	1.3 ± 0.2
Trailing Phase heterogeneous	60	2	$(2.9 \pm 0.8) \times 10^{-1}$	$(3.2 \pm 0.6) \times 10^{-1}$	0.9 ± 0.4
	60	4	$(6.1 \pm 0.9) \times 10^{-1}$	$(5.8 \pm 0.7) \times 10^{-1}$	1.1 ± 0.3
	90	2	1.7 ± 0.2	1.6 ± 0.2	1.1 ± 0.3
	90	4	0.8 ± 0.4	0.9 ± 0.3	0.9 ± 0.7

4.4 Dissolution of the heterogeneities

Residues of dissolution obtained at the end of the dissolution test in 2 mol.L^{-1} HNO_3 at 90 °C in Fig. 7 (later referred as types I and II residues) were centrifuged then washed twice with water and once with ethanol before being dried in an oven at 60 °C. The obtained residues have been characterized by SEM (Fig. 8) and their stoichiometry has been measured by X-EDS, evidencing two groups of residues corresponding to the two kinds of heterogeneities present in Pe1 pellets (Table 2).

All the observed residues are rather large, with a characteristic size of several tens of microns, with residues resulting from $U_{0.41}Th_{0.59}O_2$ heterogeneities (Fig. 8a to 8f, referred to as type I residues). They are associated to greater dissolution progress compared to the residues obtained from $U_{0.22}Th_{0.78}O_2$ heterogeneities (Fig. 8g to 8l, referred to as type II residues) as shown by their very porous appearance. Their size could either mean that smaller particles were entirely dissolved or could not be recovered using the methodology of this work. The partly dissolved heterogeneities show preferential dissolution zones, the dissolution appearing to take place mainly in the grain boundaries.

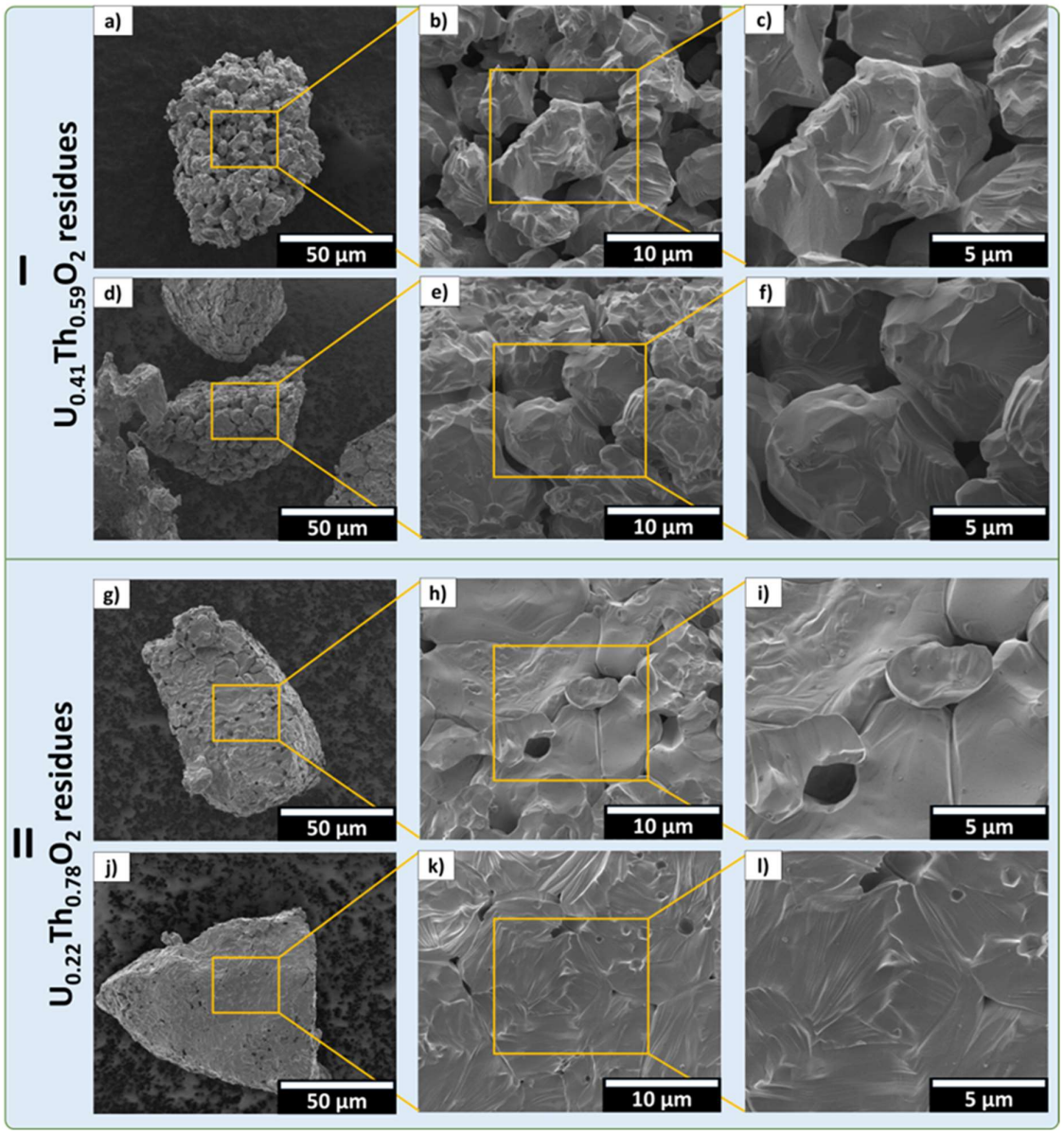

Fig. 8. SEM micrographs of the residues collected after the dissolution of heterogeneous $U_{0.68}Th_{0.32}O_2$ pellets containing 10.4 mol.% of heterogeneities in 2 mol.L^{-1} HNO_3 at 90 °C. Type I residues correspond to $U_{0.41}Th_{0.59}O_2$ heterogeneities ((a), (b), (c), (d), (e) and (f)) and type II residues correspond to $U_{0.22}Th_{0.78}O_2$ heterogeneities ((g), (h), (i), (j), (k) and (l)) as measured by X-EDS.

The specific dissolution rates of the $U_{0.41}Th_{0.59}O_2$ and $U_{0.22}Th_{0.78}O_2$ have been investigated separately. With this aim, specific dissolution tests were carried in 2 mol.L^{-1} HNO_3 at 90 °C on about 30 mg of $U_{0.41}Th_{0.59}O_2$ and $U_{0.22}Th_{0.78}O_2$ powders sintered at 1600 °C to mimic the dissolution of heterogeneities (Fig. 9). After almost 15 days of dissolution, UO_2 pellets (180 mg, 84 % theoretical density) were immersed in the solutions. This was done to rapidly add a large quantity of HNO_2 catalytic species as, according to the literature, dissolution of UO_2 induces the production of an equimolar quantity of HNO_2 in the solution [30]. As uranium was added separately to simulate the dissolution of the matrix, the dissolution of the homogeneous powders was measured using the evolution of the thorium concentration in solution.

The initial dissolution rate of $U_{0.41}Th_{0.59}O_2$ sintered powder (Fig. 9a, 3.6 wt.%.d^{-1}) was found to be linear and 7 times faster than that measured for $U_{0.22}Th_{0.78}O_2$ sintered powder (Fig. 9b, 0.5 wt.%.d^{-1}). However, this difference was significantly reduced (to a factor of 2, i.e. 17.4 wt.%.d^{-1} and 7.8 wt.%.d^{-1} for $U_{0.41}Th_{0.59}O_2$ and $U_{0.22}Th_{0.78}O_2$, respectively) after the introduction of HNO_2 catalytic species in solution resulting from the dissolution of the added UO_2 pellets. Interestingly, for both systems the dissolution rates finally decreased before returning to the initial values. This was probably due to a large decrease of HNO_2 concentration once it was not produced by the dissolution of UO_2 anymore and returned to the concentration of dynamic equilibrium with NOx gases [25]. In these conditions, the UO_2 pellets were fully dissolved in few hours.

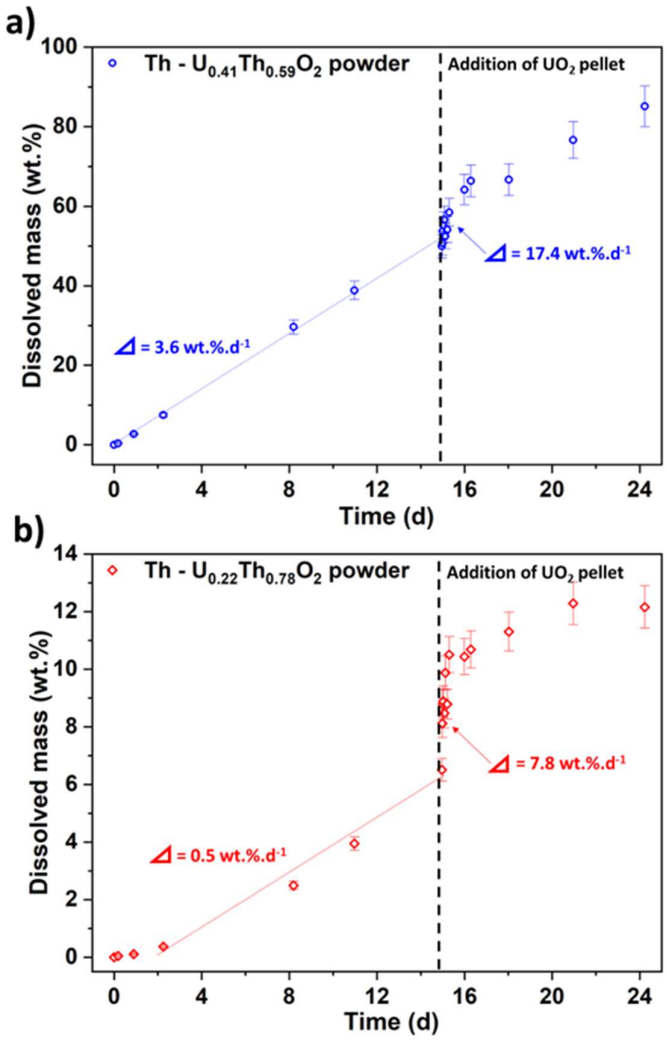

Fig. 9. Evolution of the dissolved mass of Th, Δm(t) obtained from thorium release during the dissolution in 2 mol.L^{-1} HNO_3 at 90 °C of (a) $U_{0.41}Th_{0.59}O_2$ and (b) $U_{0.22}Th_{0.78}O_2$ homogeneous powders heated at 1600 °C. ◿ refers to the slope of the dissolution curve. The dash lines point out the addition of the UO_2 pellet in the system.

4.5 Operando monitoring of the dissolution

A difference in the dissolution rates of the different phases would create preferential dissolution zones on the surface of an heterogeneous pellet. Such an expected effect resulting from the different normalized dissolution rates of the matrix and the embedded heterogeneities, could be directly observed at the microscopic scale only. Indeed, it was therefore studied through an *operando* monitoring of the dissolution (Fig. 10) of an heterogeneous $U_{0.68}Th_{0.32}O_2$ pellet (Pe1 type) in 2 mol.L^{-1} HNO_3 at 60 °C, following the methodology already described by Cordara *et al.* [43].

Before the beginning of the reaction (Fig. 10a), it was not possible to identify the matrix and heterogeneities in terms of dissolution progress. After 16 hours of dissolution (Fig. 10b), the matrix was slightly dissolved while heterogeneities kept their initial polished surface. In this figure, the orange arrow points out undissolved heterogeneity. The matrix dissolved according to a front of dissolution with seemingly preferential dissolution zones, as evidenced by the orange circle. The area circled in orange reacted faster and quickly expanded as the reaction progresses. It is worth noting that some heterogeneities seemed to break away from the microstructure after the dissolution of the matrix. The heterogeneity zone pointed by the orange arrow disappeared after 108 hours of dissolution (Fig. 10d) whereas it had retained its initial polished surface after 44 hours of dissolution (Fig. 10c).

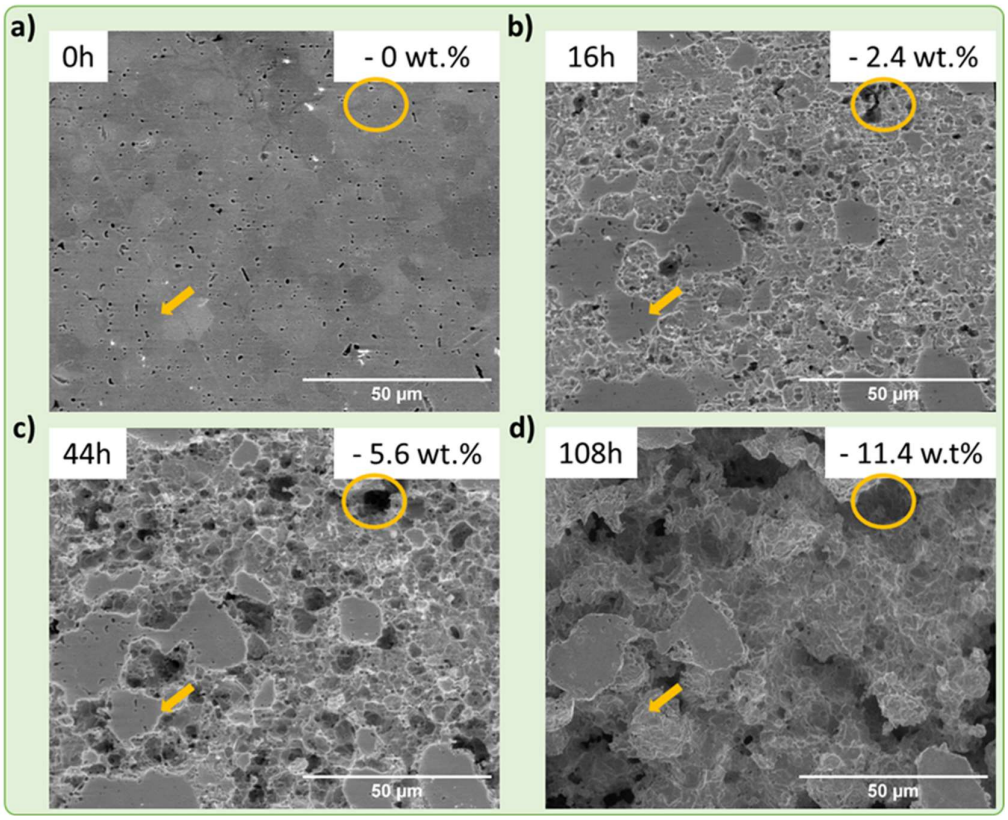

Fig. 10. ESEM micrographs of the surface of $U_{0.68}Th_{0.32}O_2$ heterogeneous pellet (Pe1 type) dissolved in 2 mol.L^{-1} HNO_3 at 60 °C for various dissolution times: (a) initial surface, (b) 16 hours, (c) 44 hours and (d) 108 hours corresponding to 0 wt.%, 2.4 wt.%, 5.6 wt.% and 11.4 wt.% of relative dissolution, respectively. For interpretation of the references to colour in this figure, the reader is referred to the web version of this article.

4.6 Effect of the incorporation rate of heterogeneities

To evidence the effect of the incorporation rate of heterogeneities in the samples, a series of experiments were performed on pellets with incorporation rates (0 to 25 mol.%) of $U_{0.22}Th_{0.78}O_2$ heterogeneities . The pellets used for these tests correspond to the simplified two powders population pellets whose microstructural characteristics have been discussed before (see Fig. 4 and Table 4). The large differences in terms of porosity and S_{SA}, as well as the variations in the stoichiometry between the pellets due to the incorporation of heterogeneities, required to use of normalized weight losses N_L (in $g.m^{-2}$) instead of dissolved masses (in $wt.\%.d^{-1}$). The evolution of the normalized weight losses of uranium obtained during the dissolution of these pellets in 2 $mol.L^{-1}$ HNO_3 at 60 °C is presented in Fig. 11a. Table 6 gathers the normalized dissolution rates R_L (in $g.m^{-2}.d^{-1}$) determined from uranium and thorium releases as well as the congruence ratio for this set of experiments. This table also depicts the dissolution rates for U and Th compared to the dissolution rate of the same elements for the homogeneous pellet (Fig. 11b).

The shapes of the curves were similar for all the tested materials. However, the measured dissolution rates were found to be greatly affected by the quantity of heterogeneities. Dissolution rates of the sample containing 5.2 mol.% of heterogeneities decreased by about 40% compared to the homogeneous pellet . The R_L values then decreased continuously but more slowly for pellets showing higher incorporation rates. If the only effect of the heterogeneities was to reduce the available surface, one could have expected to observe a linear decrease of the normalized dissolution rates with the incorporation rate as shown by the dash line in Fig. 11b. That is, an addition of 10 mol.% of heterogeneities would lead to a 10% reduction of the initial surface area of the matrix and thus to a 10% reduction of the initial dissolution rate of the pellet, providing that only the matrix is dissolving so early in the experiment. Thus, the variation of the dissolutions rates versus the heterogeneities content did not follow this linear expected trend even if a small quantity of heterogeneities largely impacted the normalized dissolution rates (Table 6).

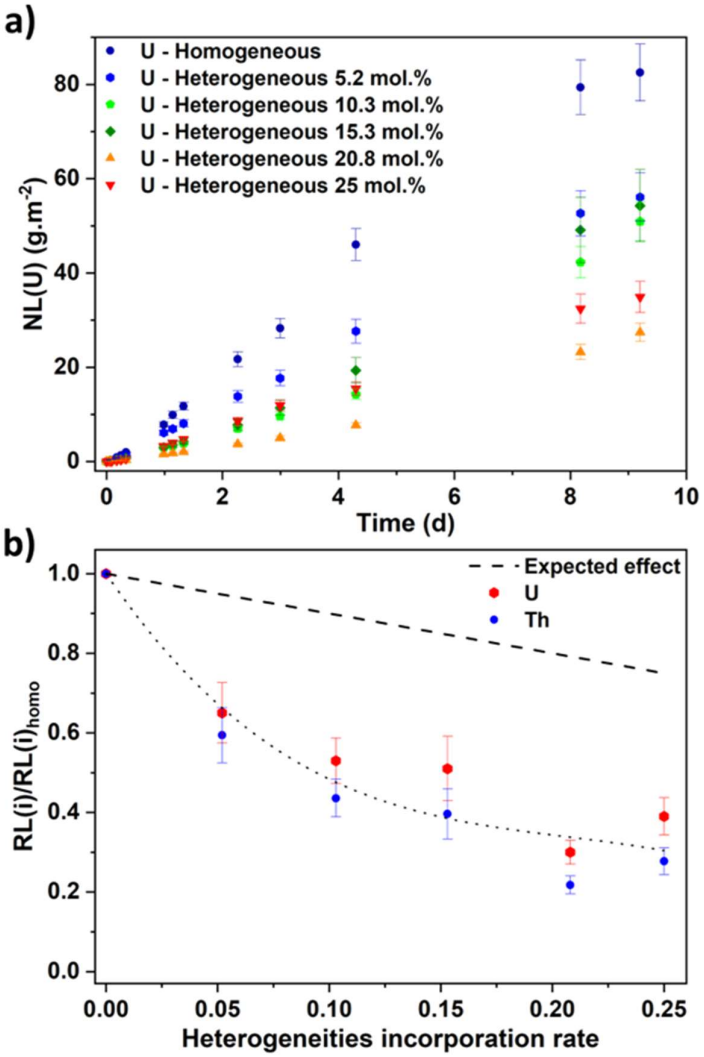

Fig. 11. Evolution of (a) the normalized weight losses $N_L(U,t)$ during the dissolution of heterogeneous $U_{1-X}Th_XO_2$ pellets containing various amounts of heterogeneities in 2 mol.L^{-1} HNO_3 at 60 °C and (b) comparison of $R_L(i = U,Th)$ versus $R_L(i)$ obtained for the homogeneous $U_{0.72}Th_{0.28}O_2$ sample. Results obtained for homogeneous $U_{0.72}Th_{0.28}O_2$ sample are included as reference material. Dotted line refers to the general tendency considering the experimental data.

Table 6. Normalized dissolution rates $R_L(t)$ obtained from U and Th releases and congruence ratios obtained during the dissolution of heterogeneous $U_{1-X}Th_XO_2$ pellets containing various amounts of heterogeneities (0-25 mol.%) in 2 mol.L^{-1} HNO_3 at 60 °C.

Sample	Heterogeneities (mol.%)	$R_{L,0}(U)$ ($g.m^{-2}.d^{-1}$)	$R_{L,0}(Th)$ ($g.m^{-2}.d^{-1}$)	r (U/Th)	$R_L(U)/R_L(U)_{homo}$	$R_L(Th)/R_L(Th)_{homo}$
Pe2	-	10.0 ± 0.7	10.1 ± 0.7	1.0 ± 0.1	1	1
Pe3	5.2	6.5 ± 0.6	6.0 ± 0.5	1.1 ± 0.1	0.65 ± 0.08	0.59 ± 0.07
Pe4	10.3	5.3 ± 0.4	4.4 ± 0.4	1.2 ± 0.1	0.53 ± 0.06	0.44 ± 0.05
Pe5	15.3	5.1 ± 0.7	4.0 ± 0.6	1.3 ± 0.2	0.51 ± 0.08	0.40 ± 0.06
Pe6	20.8	3.0 ± 0.2	2.2 ± 0.2	1.4 ± 0.2	0.30 ± 0.03	0.22 ± 0.02
Pe7	25.0	3.9 ± 0.4	2.8 ± 0.3	1.4 ± 0.2	0.39 ± 0.05	0.28 ± 0.03

5. Discussion

Major differences were observed between the dissolution of heterogeneous pellets and that of the homogeneous sample in 2 mol.L^{-1} HNO_3 at 60 °C. First of all, a decrease in the kinetics of dissolution was observed whatever the domain considered (steady state and trailing phase) for heterogeneous sample compared to the homogenous material. This has been observed whatever the content of heterogeneities present in the material. This effect was enhanced during the trailing phase, where the ratio between the dissolution rates of heterogeneous samples compared to the homogeneous sample increased from 2 to 3 (Table 5). That led to the incomplete dissolution of the heterogenous pellets. Based on the dissolution rate measured during the trailing phase (0.3 wt.%.d^{-1} for heterogeneous pellet in 2 mol.L^{-1} at 60 °C, Table 5), the time required to reach complete dissolution would be 110-135 days.

However, it is not at all certain that the reaction would have reached complete dissolution given the presence of refractory heterogeneities. In this field, residues observed in more aggressive media (2 mol.L^{-1} HNO_3 at 90 °C) more representative of reprocessing conditions were characterized (Fig. 8). This underlined a stronger resistance of such residues to dissolution compared to the matrix. Moreover, thorium enriched heterogeneities showed preferential dissolution zones (Fig. 8) mainly located in the grain boundaries, leading to a raspberry-like surface structure for $U_{0.41}Th_{0.59}O_2$ residues (Fig. 8a to 8f). Conversely, the embedding matrix dissolved more homogeneously. This remind the existence of cracking core model, when the time for the dissolution front to reach the center of the particle was significantly shorter than the time to dissolve a single grain according to the shrinking sphere model [45].

This change in terms of dissolution mechanism for high thorium content agrees well with the existence of a dissolution rate gap between thorium-enriched and uranium-enriched solid solutions, as already described by Zimmer and Merz [23]. It was explained by Claparede *et al.* [17] as a significant change from a mechanism involving the rapid oxidation of U(IV) into U(VI) at the solid/liquid interface to a mechanism mainly driven by surface reactions. This effect is enhanced for $U_{0.22}Th_{0.78}O_2$ residues, for which a very low progress of the dissolution was observed. It has been confirmed by comparing the dissolution of $U_{0.41}Th_{0.59}O_2$ and $U_{0.22}Th_{0.78}O_2$ sintered powders alone in 2 mol.L^{-1} at 90 °C (Fig. 9). Indeed, $U_{0.41}Th_{0.59}O_2$ was found to dissolve 7 times faster than $U_{0.22}Th_{0.78}O_2$ and 5 times slower than the embedding matrix ($U_{0.72}Th_{0.28}O_2$). Considering these chemical compositions, the production of nitrous acid HNO_2 is too low to induce catalytic effect during the dissolution [15].

To highlight the contribution of matrix dissolution on the dissolution kinetics of heterogeneities, a pellet of UO_2 was introduced during the dissolution of powdered samples of $U_{0.41}Th_{0.59}O_2$ and $U_{0.22}Th_{0.78}O_2$. The production of HNO_2 following the dissolution of the UO_2 pellet shows a significant impact on the dissolution kinetics of heterogeneities. Indeed, dissolution rates increased by a factor of 5 and 15 for samples $U_{0.41}Th_{0.59}O_2$ and $U_{0.22}Th_{0.78}O_2$, respectively, compared to dissolution test with no UO_2 pellet. Such an observation appears to be of strong interest in the field of the dissolution of heterogeneous MOX fuels, for which plutonium enriched residues could accumulate in the dissolution device.

Interestingly, the evolution of the dissolution rate as a function of the rate of incorporation of heterogeneities (Fig. 11b) does not follow the expected linear trend. Indeed, even in the presence of small amounts of heterogeneities (up to 10.3 mol.%), a clear decrease of the dissolution rate of the heterogeneous solid compared to the homogeneous material is observed. This slowdown remains present but less important when more heterogeneities are added in the sample.

This effect is counterintuitive given the previously mentioned description of the dissolution where most of the dissolution can be attributed to the embedding matrix. One possible explanation would be the possible effect of crystallite size of the different phases (ie the matrix and the heterogeneities) due to their different heating temperature which could, despite being sintered together at 1700 °C, partly explain the effect observed in Fig. 11b. However, Claparede et al. previously observed that the dissolution rate is fairly independent of the crystallite size for heating temperatures higher than 900 °C [17]. Another explanation would be that heterogeneities could hinder the dissolution reaction of the embedding matrix and slow down the development of the surface, which is the main contributing parameter to the increase of the dissolution rate. This would explain the presence of a small lag observed during the dissolution of the heterogeneous sample compared to the homogeneous solid solution (Fig. 5). Testing this hypothesis requires a more detailed study of the dissolution at the microscopic scale, including for example the quantification of local dissolution rates as well as the study of evolving solid-solution interface during dissolution.

The *operando* monitoring of the dissolution (Fig. 10) clearly shows the existence of heterogeneous dissolution at the solid/solution interface, with preferential dissolution of the embedding matrix compared to the thorium enriched heterogeneities. This behavior induces a specific evolution of the reactive surface in the presence of heterogeneities. In this field, working on homogeneous samples, Fukasawa and Osawa [46] proposed a gradual increase of the reactive surface area until a maximum of around 3.5 times the initial surface for 40 wt.% of solid dissolved before decreasing to 0 when all the solid has been dissolved. Moreover, Horlait *et al*. also observed an increase by a factor of 20-30 of the surface area during dissolution of $Ce_{0.24}Nd_{0.76}O_{1.62}$ in 4 mol.L^{-1} HNO_3, which has been confirmed by BET measurement [38]. Such an effect could be enhanced for heterogeneous materials due to the development of cavities and interconnected porosities, associated to the remaining refractory heterogeneities. This important point should be studied in depth through the development of complementary experiments. This study highlights the needs for complementary experiments, focused on links between the physico-chemical and microstructural properties of the matrix-inclusions interaction (for instance, distribution of heterogeneities, role of the interphase, …) and the consequences observed in terms of normalized dissolution rates.

6. Conclusion

The aim of this study was to analyze the impact of thorium enriched heterogeneities during the dissolution of heterogeneous $U_{1-x}Th_xO_2$ pellets showing a matrix-inclusion microstructure. In this field, the preparation, the characterization then study of the chemical durability of several samples containing different contents of heterogeneities were performed in various experimental conditions, including the operando monitoring of the solid/liquid interface. The coupling of wet and solid synthesis methods allowed the preparation of heterogeneous model compounds whose surface occupied by the heterogeneities is close to the target values.

Major differences were observed between the dissolution of heterogeneous and homogeneous pellets in 2 mol.L^{-1} HNO_3 at 60 °C. Indeed, the uranium enriched matrix dissolved more rapidly than the refractory thorium enriched heterogeneities as evidenced by operando monitoring of the dissolution. Such a difference in chemical durability leads to the presence of dissolution residues. Their characterization by SEM showed notable differences in dissolution progress depending on the chemical composition of the heterogeneities. It is also important to note that the kinetics of dissolution of heterogeneities is sensitive to the presence of catalytic HNO_2 linked to the dissolution of the matrix. The dissolution rate of the uranium enriched matrix phase seemed to be affected by the presence of

refractory heterogeneities. Indeed, even small amounts of heterogeneities (up to 10.3 mol.%) decrease sharply the dissolution rate of the heterogeneous solid compared to the homogeneous material.

This slowdown remains present but less important when more heterogeneities are added in the sample. The origin of their effect was probably microstructural, heterogeneities leading to a difference in the evolution of surface area during the dissolution.

Acknowledgement

The authors are grateful to Joseph Lautru and Béatrice Baus-Lagarde (ICSM) for their help in SEM and ICP-OES analyses as well as Orano and EDF for their financial support.

Supplementary information

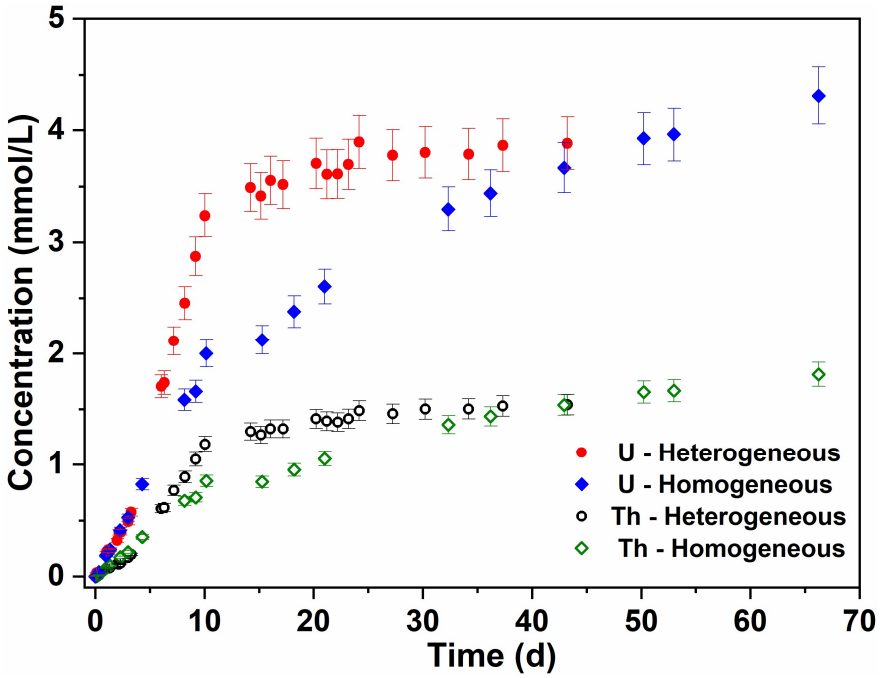

Fig. 12. Evolution of the elemental concentration of uranium and thorium during the dissolution of an homogeneous $U_{0.72}Th_{0.28}O_2$ pellet and an heterogeneous $U_{0.68}Th_{0.32}O_2$ containing 10.4 mol.% of heterogeneities at 60 °C in 2 mol.L^{-1} HNO_3. The steady state and trailing phase steps, as described by Dalger *et al.* [15], are outlined.

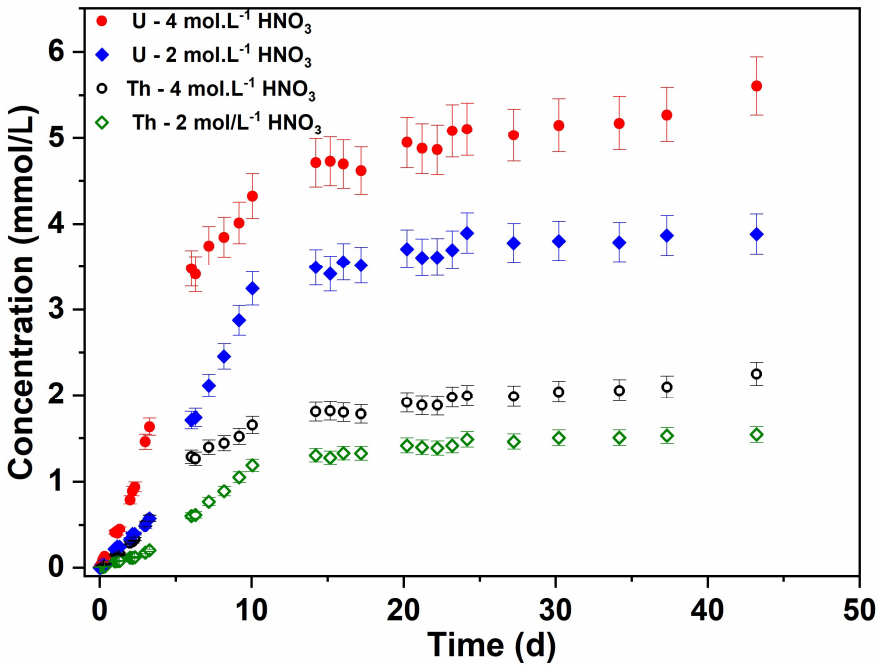

Fig. 13. Evolution of the elemental concentration of uranium and thorium during the dissolution of heterogeneous $U_{0.68}Th_{0.32}O_2$ pellets containing 10.4 mol.% of heterogeneities in 2 and 4 mol.L^{-1} HNO_3 at 60 °C.

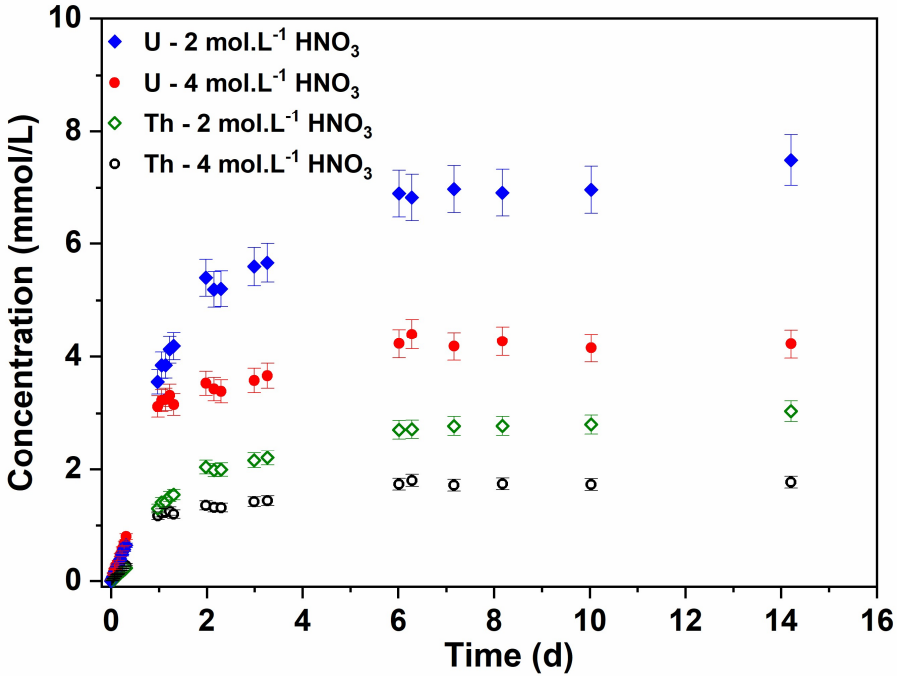

Fig. 14. Evolution of the elemental concentration of uranium and thorium during the dissolution of heterogeneous $U_{0.68}Th_{0.32}O_2$ pellets containing 10.4 mol.% of heterogeneities in 2 and 4 mol.L^{-1} HNO_3 at 90 °C.

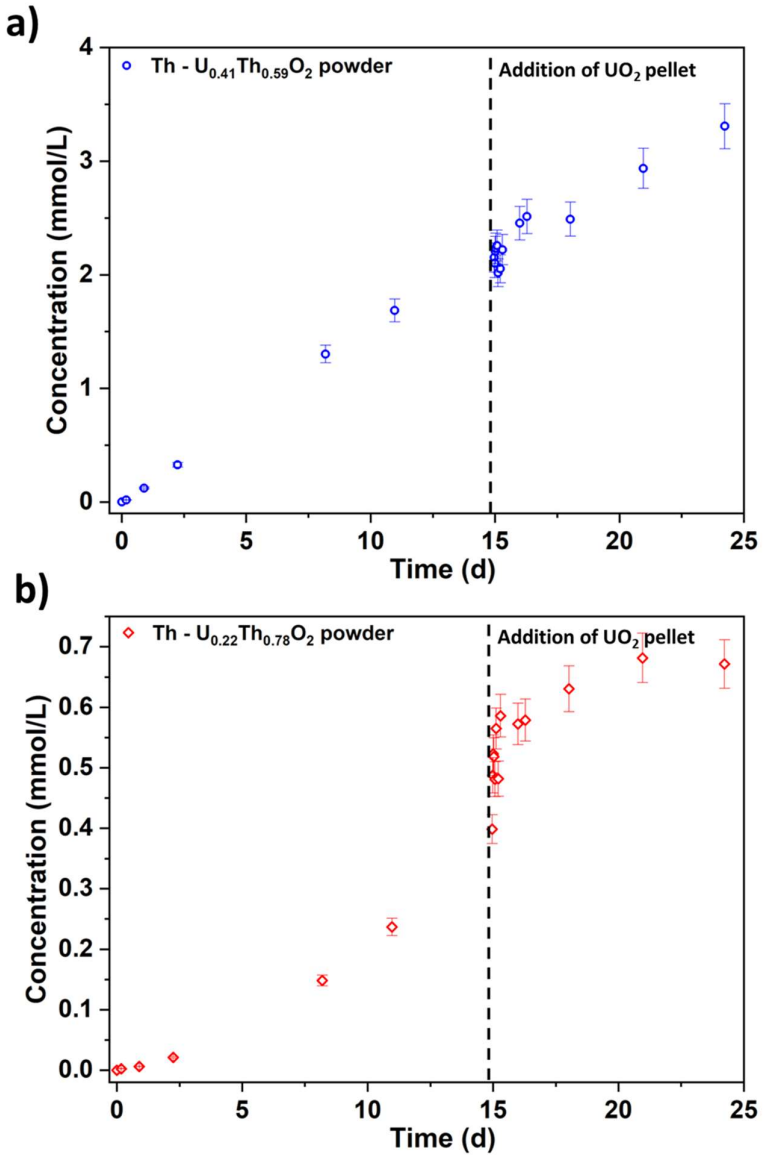

Fig. 15. Evolution of the concentration of Th obtained from thorium release during the dissolution in 2 mol.L^{-1} HNO_3 at 90 °C of (a) $U_{0.41}Th_{0.59}O_2$ and (b) $U_{0.22}Th_{0.78}O_2$ homogeneous powders heated at 1600 °C.

References

[1] A.L. Uriarte, R.H. Rainey, Dissolution of High-density UO2, PuO2, and UO2-PuO2 Pellets in Inorganic Acids, Oak Ridge National Laboratory, 1965.

[2] D. Vollath, H. Wedemeyer, H. Elbel, E. Günther, On the Dissolution of (U,Pu)O2 Solid Solutions with Different Plutonium Contents in Boiling Nitric Acid, Nucl. Technol. 71 (1985) 240–245. https://doi.org/10.13182/NT85-A33723.

[3] T. Truphémus, R.C. Belin, J.-C. Richaud, M. Reynaud, M.-A. Martinez, I. Félines, A. Arredondo, A. Miard, T. Dubois, F. Adenot, J. Rogez, Structural studies of the phase separation in the UO2–PuO2–Pu2O3 ternary system, J. Nucl. Mater. 432 (2013) 378–387. https://doi.org/10.1016/j.jnucmat.2012.07.034.

[4] R. Parrish, A. Aitkaliyeva, A review of microstructural features in fast reactor mixed oxide fuels, J. Nucl. Mater. 510 (2018) 644–660. https://doi.org/10.1016/j.jnucmat.2018.05.076.

[5] CEA, 4th-Generation Sodium-Cooled Fast Reactors : The Astrid Technological Demonstrator, 2012.

[6] K. Tirel, T. Kooyman, C. Coquelet-Pascal, E. Merle, Possibility to stabilize plutonium inventory in a sodium-cooled small modular reactors – Pressurized water reactors fleet, Ann. Nucl. Energy. 146 (2020) 107632. https://doi.org/10.1016/j.anucene.2020.107632.

[7] D. Staicu, Thermal Properties of Irradiated UO2 and MOX, in: R.J.M. Konings (Ed.), Compr. Nucl. Mater., Elsevier, 2012: pp. 439–464.

[8] P. Van Uffelen, G. Pastore, Oxide Fuel Performance Modeling and Simulation, in: R.J.M. Konings, R.E. Stoller (Eds.), Compr. Nucl. Mater. Second Ed., Elsevier, Oxford, 2020: pp. 363–416.

[9] M.D. Freshley, Mixed-Oxide Fuel Irradiations in the Plutonium Recycle Test Reactor, Nucl. Technol. 15 (1972) 125–176. https://doi.org/10.13182/NT72-A31143.

[10] I.L. Jenkins, P.E. Brown, Characterisation of Dissolution Residues — Fuel Element Cladding and Fission Product Insolubles, Radiochim. Acta. 36 (1984) 25–30.

[11] H. Aihara, Y. Arai, A. Shibata, K. Nomura, M. Takeuchi, Characterization of the Insoluble Sludge from the Dissolution of Irradiated Fast Breeder Reactor Fuel, Procedia Chem. 21 (2016) 279–284. https://doi.org/10.1016/j.proche.2016.10.039.

[12] M.J. Carrott, P.M.A. Cook, O.D. Fox, C.J. Maher, S.L.M. Schroeder, The Chemistry of (U,Pu)O2 Dissolution in Nitric Acid, Procedia Chem. 7 (2012) 92–97. https://doi.org/10.1016/j.proche.2012.10.017.

[13] N. Desigan, S. Ganesh, N.K. Pandey, Dissolution behavior of fast reactor MOX nuclear fuel pellets in nitric acid medium, J. Nucl. Mater. 554 (2021) 153077. https://doi.org/10.1016/j.jnucmat.2021.153077.

[14] R.E. Lerch, Dissolution of mixed oxide fuel as a function of fabrication variables, Hanford Engineering Development Laboratory, 1979.

[15] T. Dalger, S. Szenknect, F. Tocino, L. Claparede, A. Mesbah, P. Moisy, N. Dacheux, Kinetics of dissolution of Th0.25U0.75O2 sintered pellets in various acidic conditions, J. Nucl. Mater. 510 (2018) 109–122. https://doi.org/10.1016/j.jnucmat.2018.07.050.

[16] C.L. Corkhill, E. Myllykylä, D.J. Bailey, S.M. Thornber, J. Qi, P. Maldonado, M.C. Stennett, A. Hamilton, N.C. Hyatt, Contribution of Energetically Reactive Surface Features to the Dissolution of CeO2 and ThO2 Analogues for Spent Nuclear Fuel Microstructures, ACS Appl. Mater. Interfaces. 6 (2014) 12279–12289. https://doi.org/10.1021/am5018978.

[17] L. Claparede, F. Tocino, S. Szenknect, A. Mesbah, N. Clavier, P. Moisy, N. Dacheux, Dissolution of Th1−xUxO2: Effects of chemical composition and microstructure, J. Nucl. Mater. 457 (2015) 304–316. https://doi.org/10.1016/j.jnucmat.2014.11.094.

[18] L. Claparede, N. Clavier, A. Mesbah, F. Tocino, S. Szenknect, J. Ravaux, N. Dacheux, Impact of the cationic homogeneity on Th0.5U0.5O2 densification and chemical durability, J. Nucl. Mater. 514 (2019) 368–379. https://doi.org/10.1016/j.jnucmat.2018.12.009.

[19] N. Desigan, D. Maji, K. Ananthasivan, N.K. Pandey, U. Kamachi Mudali, J.B. Joshi, Dissolution behaviour of simulated MOX nuclear fuel pellets in nitric acid medium, Prog. Nucl. Energy. 116 (2019) 1–9. https://doi.org/10.1016/j.pnucene.2019.03.027.
[20] G.T. Seaborg, Overview of the Actinide and Lanthanide (the f) Elements, Radiochim. Acta. 61 (1993) 115–122. https://doi.org/10.1524/ract.1993.61.34.115.
[21] S. Hubert, K. Barthelet, B. Fourest, G. Lagarde, N. Dacheux, N. Baglan, Influence of the precursor and the calcination temperature on the dissolution of thorium dioxide, J. Nucl. Mater. 297 (2001) 206–213. https://doi.org/10.1016/S0022-3115(01)00604-3.
[22] H.-D. Greiling, K.H. Lieser, Properties of ThO2 , UO2 and PuO2 as Function of Pretreatment and their Dissolution in HNO3., Radiochim. Acta. 35 (1984) 79–90. https://doi.org/10.1524/ract.1984.35.2.79.
[23] E. Zimmer, E. Merz, Dissolution of thorium-uranium mixed oxides in concentrated nitric acid, J. Nucl. Mater. 124 (1984) 64–67. https://doi.org/10.1016/0022-3115(84)90010-2.
[24] A. Inoue, Mechanism of the oxidative dissolution of UO2 in HNO3 solution, J. Nucl. Mater. 138 (1986) 152–154. https://doi.org/10.1016/0022-3115(86)90271-0.
[25] J.Y. Park, Y.N. Lee, Solubility and decomposition kinetics of nitrous acid in aqueous solution, J. Phys. Chem. 92 (1988) 6294–6302. https://doi.org/10.1021/j100333a025.
[26] F. Charlier, D. Canion, A. Gravinese, A. Magnaldo, S. Lalleman, G. Borda, E. Schaer, Formalization of the kinetics for autocatalytic dissolutions. Focus on the dissolution of uranium dioxide in nitric medium, EPJ Nucl. Sci. Technol. 3 (2017) 26. https://doi.org/10.1051/epjn/2017018.
[27] P. Marc, A. Magnaldo, A. Vaudano, T. Delahaye, É. Schaer, Dissolution of uranium dioxide in nitric acid media: what do we know?, EPJ Nucl. Sci. Technol. 3 (2017) 13. https://doi.org/10.1051/epjn/2017005.
[28] M. Shabbir, R.G. Robins, Kinetics of the dissolution of uranium dioxide in nitric acid. I, J. Appl. Chem. 18 (1968) 129–134. https://doi.org/10.1002/jctb.5010180501.
[29] M. Shabbir, R.G. Robins, Kinetics of the dissolution of uranium dioxide in nitric acid. II, J. Appl. Chem. 19 (1969) 52–56. https://doi.org/10.1002/jctb.5010190205.
[30] T. Cordara, S. Szenknect, L. Claparede, R. Podor, A. Mesbah, C. Lavalette, N. Dacheux, Kinetics of dissolution of UO2 in nitric acid solutions: A multiparametric study of the non-catalysed reaction, J. Nucl. Mater. 496 (2017) 251–264. https://doi.org/10.1016/j.jnucmat.2017.09.038.
[31] R. Podor, X. Le Goff, T. Cordara, M. Odorico, J. Favrichon, L. Claparede, S. Szenknect, N. Dacheux, 3D-SEM height maps series to monitor materials corrosion and dissolution, Mater. Charact. 150 (2019) 220–228. https://doi.org/10.1016/j.matchar.2019.02.017.
[32] J. Martinez, A. Mesbah, F. Audubert, X. Le Goff, N. Vigier, N. Dacheux, N. Clavier, An original precipitation route toward the preparation and the sintering of highly reactive uranium cerium dioxide powders, J. Nucl. Mater. (2015) 173–181. https://doi.org/10.1016/j.jnucmat.2015.03.053.
[33] N. Dacheux, V. Brandel, M. Genet, Snythesis and properties of uranium chloride phosphate tetrahydrate : UClPO4.4H2O, New J Chem. 19 (1995) 1029–1036. https://doi.org/1144-0546/95/10.
[34] H. Xiao, C. Long, X. Tian, H. Chen, Effect of thorium addition on the thermophysical properties of uranium dioxide: Atomistic simulations, Mater. Des. 96 (2016) 335–340. https://doi.org/10.1016/j.matdes.2016.02.019.
[35] L. Balice, D. Bouëxière, M. Cologna, A. Cambriani, J.-F. Vigier, E. De Bona, G.D. Sorarù, C. Kübel, O. Walter, K. Popa, Nano and micro U1-xThxO2 solid solutions: From powders to pellets, J. Nucl. Mater. 498 (2018) 307–313. https://doi.org/10.1016/j.jnucmat.2017.10.042.
[36] W. Trzebiatowski, P.W. Selwood, Magnetic Susceptibilities of Urania-Thoria Solid Solutions, J. Am. Chem. Soc. 72 (1950) 4504–4506. https://doi.org/10.1021/ja01166a046.
[37] M. Kanno, S. Kokubo, H. Furuya, Preparation of Thorium-Uranium Mixed Oxide Pellets, J. Nucl. Sci. Technol. 19 (1982) 956–958. https://doi.org/10.1080/18811248.1982.9734242.

[38] D. Horlait, L. Claparede, F. Tocino, N. Clavier, J. Ravaux, S. Szenknect, R. Podor, N. Dacheux, Environmental SEM monitoring of Ce1−xLnxO2−x/2 mixed-oxide microstructural evolution during dissolution, J. Mater. Chem. A. 2 (2014) 5193–5203. https://doi.org/10.1039/C3TA14623E.
[39] P. Thévenaz, M. Unser, User-friendly semiautomated assembly of accurate image mosaics in microscopy, Microsc. Res. Tech. 70 (2007) 135–146. https://doi.org/10.1002/jemt.20393.
[40] A.C. Lasaga, A. Lüttge, A model for crystal dissolution, Eur. J. Mineral. (2003) 603–615. https://doi.org/10.1127/0935-1221/2003/0015-0603.
[41] C.L. Corkhill, D.J. Bailey, F.Y. Tocino, M.C. Stennett, J.A. Miller, J.L. Provis, K.P. Travis, N.C. Hyatt, Role of Microstructure and Surface Defects on the Dissolution Kinetics of CeO2, a UO2 Fuel Analogue, ACS Appl. Mater. Interfaces. 8 (2016) 10562–10571. https://doi.org/10.1021/acsami.5b11323.
[42] S. Bertolotto, S. Szenknect, S. Lalleman, A. Magnaldo, P. Raison, M. Odorico, R. Podor, L. Claparede, N. Dacheux, Effect of surface orientation on dissolution rate and surface dynamics of UO2 single crystals in nitric acid, Corros. Sci. 176 (2020) 109020. https://doi.org/10.1016/j.corsci.2020.109020.
[43] T. Cordara, S. Szenknect, R. Podor, V. Trillaud, L. Claparede, X. Le Goff, A. Mesbah, C. Lavalette, N. Dacheux, Microstructural evolution of UO2 pellets containing metallic particles of Ru, Rh and Pd during dissolution in nitric acid solution: 3D-ESEM monitoring, Hydrometallurgy. 188 (2019) 182–193. https://doi.org/10.1016/j.hydromet.2019.07.001.
[44] T. Dalger, L. Claparede, S. Szenknect, P. Moisy, N. Dacheux, Dissolution of Th0.25U0.75O2 sintered pellets: Impact of nitrate ions and nitrous acid, Hydrometallurgy. 204 (2021) 105717. https://doi.org/10.1016/j.hydromet.2021.105717.
[45] J.Y. Park, O. Levenspiel, The crackling core model for the reaction of solid particles, Chem. Eng. Sci. 30 (1975) 1207–1214. https://doi.org/10.1016/0009-2509(75)85041-X.
[46] T. Fukasawa, Y. Ozawa, Relationship between dissolution rate of uranium dioxide pellets in nitric acid solutions and their porosity, J. Radioanal. Nucl. Chem. 106 (1986) 345–356. https://doi.org/10.1007/BF02163667.